



NAVAL POSTGRADUATE SCHOOL

MONTEREY, CALIFORNIA

THESIS

**NEAR FIELD IMAGING FOR THE CHARACTERIZATION
OF DIFFUSION LENGTH AND WAVEGUIDING
IN ZINC OXIDE NANOWIRES**

by

Anree G. Little

June 2012

Thesis Advisor:
Second Reader:

Nancy M. Haegel
James Luscombe

Approved for public release; distribution is unlimited

THIS PAGE INTENTIONALLY LEFT BLANK

REPORT DOCUMENTATION PAGE			Form Approved OMB No. 0704-0188	
Public reporting burden for this collection of information is estimated to average 1 hour per response, including the time for reviewing instruction, searching existing data sources, gathering and maintaining the data needed, and completing and reviewing the collection of information. Send comments regarding this burden estimate or any other aspect of this collection of information, including suggestions for reducing this burden, to Washington headquarters Services, Directorate for Information Operations and Reports, 1215 Jefferson Davis Highway, Suite 1204, Arlington, VA 22202-4302, and to the Office of Management and Budget, Paperwork Reduction Project (0704-0188) Washington DC 20503.				
1. AGENCY USE ONLY (Leave blank)		2. REPORT DATE June 2012		3. REPORT TYPE AND DATES COVERED Master's Thesis
4. TITLE AND SUBTITLE Near Field Imaging for the Characterization of Diffusion Length and Waveguiding in Zinc Oxide Nanowires			5. FUNDING NUMBERS DMR 0804527	
6. AUTHOR(S) Anree G. Little				
7. PERFORMING ORGANIZATION NAME(S) AND ADDRESS(ES) Naval Postgraduate School Monterey, CA 93943-5000			8. PERFORMING ORGANIZATION REPORT NUMBER	
9. SPONSORING /MONITORING AGENCY NAME(S) AND ADDRESS(ES) National Science Foundation			10. SPONSORING/MONITORING AGENCY REPORT NUMBER	
11. SUPPLEMENTARY NOTES The views expressed in this thesis are those of the author and do not reflect the official policy or position of the Department of Defense or the U.S. Government. IRB Protocol number ____N/A____.				
12a. DISTRIBUTION / AVAILABILITY STATEMENT Approved for public release; distribution is unlimited			12b. DISTRIBUTION CODE	
13. ABSTRACT (maximum 200 words) A novel technique of near field imaging has been advanced and used to measure free carrier diffusion length and study optical waveguiding in ZnO nanowires. The technique employs a near field scanning optical microscope (NSOM) and atomic force microscope (AFM) to optically and spatially map cathodoluminescence generated by a scanning electron microscope (SEM). The technique has been advanced from previous work on nanowires by the use of a higher resolution SEM and filtering approximately 90% of any background luminescent signal directly generated in the AFM/NSOM probe. For diameters between 250 nm and 800 nm, the diffusion length was found to vary with diameter. For diameters greater than 800 nm, the diffusion length is relatively constant. This is only the second such diameter dependence measurement for ZnO nanowires, and the only measurement for this nanowire diameter range. The full width at half maximum (FWHM) of the waveguiding output distribution from a single nanowire was found to be uncorrelated with the carrier excitation rate for a 60x increase in excitation rate. Luminescence of $\lambda \approx 380$ nm was shown to propagate in the nanowire to a distance of 20-30 μm , indicating an absorption coefficient of $\sim 2000 \text{ cm}^{-1}$.				
14. SUBJECT TERMS ZnO, Near-field scanning optical microscopy, NSOM, Diameter dependence, Waveguiding, Transport imaging, Diffusion length			15. NUMBER OF PAGES 101	
			16. PRICE CODE	
17. SECURITY CLASSIFICATION OF REPORT Unclassified	18. SECURITY CLASSIFICATION OF THIS PAGE Unclassified	19. SECURITY CLASSIFICATION OF ABSTRACT Unclassified	20. LIMITATION OF ABSTRACT UU	

NSN 7540-01-280-5500

Standard Form 298 (Rev. 8-98)
Prescribed by ANSI Std. Z39.18

THIS PAGE INTENTIONALLY LEFT BLANK

Approved for public release; distribution is unlimited

**NEAR FIELD IMAGING FOR THE CHARACTERIZATION OF DIFFUSION
LENGTH AND WAVEGUIDING IN ZINC OXIDE NANOWIRES**

Anree G. Little
Lieutenant, United States Navy
B.S.E. University of Michigan, 2006

Submitted in partial fulfillment of the
requirements for the degree of

MASTER OF SCIENCE IN APPLIED PHYSICS

from the

**NAVAL POSTGRADUATE SCHOOL
June 2012**

Author: Anree G. Little

Approved by: Nancy M. Haegel
Thesis Advisor

James Luscombe
Second Reader

Andres Larraza
Chair, Department of Physics

THIS PAGE INTENTIONALLY LEFT BLANK

ABSTRACT

A novel technique of near field imaging has been advanced and used to measure free carrier diffusion length and study optical waveguiding in ZnO nanowires. The technique employs a near field scanning optical microscope (NSOM) and atomic force microscope (AFM) to optically and spatially map cathodoluminescence generated by a scanning electron microscope (SEM). The technique has been advanced from previous work on nanowires by the use of a higher resolution SEM and filtering approximately 90% of any background luminescent signal directly generated in the AFM/NSOM probe.

For diameters between 250 nm and 800 nm, the diffusion length was found to vary with diameter. For diameters greater than 800 nm, the diffusion length is relatively constant. This is only the second such diameter dependence measurement for ZnO nanowires, and the only measurement for this nanowire diameter range.

The full width at half maximum (FWHM) of the waveguiding output distribution from a single nanowire was found to be uncorrelated with the carrier excitation rate for a 60x increase in excitation rate. Luminescence of $\lambda \approx 380$ nm was shown to propagate in the nanowire to a distance of 20-30 μm , indicating an absorption coefficient of $\sim 2000 \text{ cm}^{-1}$.

THIS PAGE INTENTIONALLY LEFT BLANK

TABLE OF CONTENTS

I.	INTRODUCTION.....	1
A.	THESIS SCOPE.....	1
B.	BACKGROUND	1
	1. Trends in Electronics	1
	2. Nanowires.....	2
C.	DEFENSE RELEVANCE.....	3
D.	MICROSCOPE CONCEPTS	5
	1. Near-Field Scanning Optical Microscopy	5
	2. Atomic Force Microscopy	7
	3. Combined AFM/NSOM Probe Tip	7
E.	CATHODOLUMINESCENCE.....	8
F.	BASIC SEMICONDUCTOR PRINCIPLES.....	10
	1. Band Structure.....	10
	2. Direct and Indirect Bandgaps	11
G.	NANOWIRE GROWTH PROCESS.....	13
H.	DIFFUSION LENGTH IN ONE DIMENSION.....	15
I.	WAVEGUIDES.....	15
II.	GENERAL EXPERIMENTAL SETUP AND METHDS.....	17
A.	EXPERIMENTAL SETUP	17
	1. Overview.....	17
	2. Head Assembly	18
	a. NSOM/AFM Probe	20
	3. Computer.....	21
	4. Low Voltage Adaptor	22
	5. Photomultiplier Tube	22
	6. Counter and Power Supply	23
	7. High Voltage Piezo Driver	24
	8. Scanning Probe Microscopy (SPM) Controller	25
	9. Data Transition (DT) Interface Box.....	25
	10. Power Supply.....	25
	11. The Scanning Electron Microscope (SEM).....	26
	12. Sample.....	29
B.	EXPERIMENTAL METHOD	31
	1. Overview.....	31
	2. Lock-In Procedure	32
	3. Approaching the Sample Surface	35
	4. Initiating a Scan	36
III.	CONTROL EXPERIMENT	39
A.	OVERVIEW	39
B.	EXPERIMENTS.....	41
	1. Control Raster Scan	41

2.	Cathodoluminescence of Probe Tip.....	45
C.	FILTERS SELECTION	46
1.	Theoretical Filter Performance	47
2.	Measured Filter Effectiveness	49
3.	Filter Impact on the ZnO Cathodoluminescence Signal Received	50
IV.	DIFFUSION LENGTH MEASUREMENTS.....	53
A.	DIFFUSION LENGTH AS A FUNCTION OF NANOWIRE DIAMETER.....	53
1.	Overview	53
2.	Settings	53
3.	Method.....	53
a.	<i>Diameter Measurements</i>	53
b.	<i>Scanning Cathodoluminescence</i>	53
c.	<i>Analyzing Data</i>	54
4.	Results.....	56
V.	WAVEGUIDING EXPERIMENTS	59
A.	WAVEGUIDING AS FUNCTION OF SPOT SIZE (PROBE CURRENT).....	59
1.	Overview	59
2.	Settings	60
3.	Method.....	61
a.	<i>Waveguiding Scan</i>	61
b.	<i>Analyzing Data</i>	61
4.	Results.....	61
a.	<i>Full Width Half Maximum (FWHM)</i>	61
b.	<i>Intensity as a Function of Spot Size</i>	63
B.	WAVEGUIDING LIMIT AND ESTIMATION OF ABSORPTION COEFFICIENT	65
1.	Overview	65
2.	Settings	65
3.	Method.....	65
a.	<i>Measuring Intensity and Distance</i>	65
b.	<i>Analyzing Data</i>	65
4.	Results.....	66
a.	<i>Waveguide Limit</i>	66
b.	<i>Estimation of Absorption Coefficient</i>	66
VI.	CONCLUSIONS AND SUGGESTIONS FOR FUTURE RESEARCH.....	69
A.	CONCLUSIONS	69
B.	SUGGESTIONS FOR FUTURE RESEARCH	70
1.	Reducing Charging and Drifting in SEM.....	70
2.	Linking the ZnO Nanowire Diffusion Length Diameter Dependency Work	70
3.	Exploring Additional Materials.	71

LIST OF REFERENCES.....	73
INITIAL DISTRIBUTION LIST	77

THIS PAGE INTENTIONALLY LEFT BLANK

LIST OF FIGURES

Figure 1.	Combined AFM/NSOM probe tip. Tip includes a cantilevered tapered fiber optic wire with aperture at one end for collecting light. This is the NSOM portion of the tip and is glued to the tuning fork, which makes up the AFM portion of the tip. The AFM portion of the tip is responsible for vibrating at resonant frequency, sensing the topography of the sample, and using the feedback mechanism to maintain the probe close to the surface sample. The NSOM collects the light from the sample surface and transmits the light along the fiber optic wire. From [20]	8
Figure 2.	An electron beam incident on a semiconductor sample. Many interactions are possible and do occur. The principle focus of this thesis is on cathodoluminescence, where the electrons excite free electrons and holes. Those electrons and holes then de-excite and give off energy in the form of a photon. After [21].....	9
Figure 3.	The conduction band and valence band, separated by the bandgap. Note that metals do not have a forbidden region or bandgap; the valence band and conduction band overlap. The insulator has the largest band gap. The semiconductor has a smaller bandgap than the insulator. The Fermi level is located approximately half way through the forbidden zone. After [23].....	11
Figure 4.	Direct and indirect bandgap semiconductor material shown on an energy (E) versus momentum (k) graph. The conduction and valence bands are separated by the bandgap. For the indirect bandgap material, the momentums are not equal for the preferred transition of the electron. In order for momentum to be conserved, a phonon has to be released in addition to the photon. The direct bandgap electron de-excitation does not require a phonon as the momentums are equal. The requirement of the additional particle makes radiative capture less likely in indirect bandgap materials. Therefore, a direct bandgap material tends to luminesce more by such techniques as cathodoluminescence. After [24].....	13
Figure 5.	Thermal Evaporation process. The source material (e.g., bulk ZnO) is evaporated. A carrier gas transports the vapors to the low temperature region where it is condensed onto a substrate. After [25].....	14
Figure 6.	Basic functional block diagram of the control and instrumentation components for the Multiview 2000. After [27].....	17
Figure 7.	The Multiview 2000 head, developed by Nanonics Inc. This is the normal configuration for operation.....	19
Figure 8.	The Multiview 2000 head mounted in the chamber of the FEI Inspect F50 SEM. The AFM/NSOM probe is screwed into the upper scanner (left). The lower scanner (right) houses the sample.	

	Copper wire and tape serve to ground the instruments. This view is with the upper scanner rotated about the hinge that connects the upper and lower scanners.	20
Figure 9.	The AFM/NSOM probe. (a) The holder has an electrical grid attached to the back, which connects to the Multiview 2000 head assembly, and allows for the control of the tip. (b) On the underside of the holder, electrodes that connect the AFM tuning fork can be seen. A non-conductive glue is used to connect the tapered NSOM fiber optic wire to the end of the tuning fork. (c) The probe box contains important information about the probe such as the size of the aperture (ϕ), frequency (f), quality factor (Q), the mode (collection), and type of fiber (ultraviolet).....	21
Figure 10.	The Low Voltage Adapter is used to select either the upper or lower scanner for scanning and feedback adjustments.	22
Figure 11.	Photomultiplier tube fed by the fiber optic wire from the NSOM probe.	23
Figure 12.	Upper Left Module: High Voltage Piezo Driver for the lower stage. Lower Left Module: SPM Controller. Upper Right Module: Counter and Power Supply. Lower Right Module: High Voltage Piezo Driver for the upper stage.	24
Figure 13.	(a) System Power Supply and (b) The DT Interface.	26
Figure 14.	FEI Inspect F50 Scanning Electron Microscope. The microscope is controlled by an independent computer.....	27
Figure 15.	xT Microscope Control screenshot. The full frame, line, and spot mode are option under the Scan drop-down menu. The cross-hairs appear and the frame stops updating. The image is at 18500x magnification. The spot size is 2.0, voltage 20.0 kV. Zinc Oxide nanowire and NSOM probe tip are also shown.	28
Figure 16.	Zinc oxide (ZnO) nanostructures grown by physical vapor deposition (PVD) on silicon substrate. Sample mounted on sample holder by light adhesive. Copper tape and wire electrically grounds sample to NSOM stage.	29
Figure 17.	Zinc Oxide (ZnO) nanostructures on a silicon substrate, grown by the thermal evaporation process. Magnification is 300x, working distance is 7.8 mm, spot size of 3.0.....	30
Figure 18.	(a) ZnO nanowire, approximately 1 μ m in diameter. SEM Image taken at accelerating voltage of 30kV, magnification 50,000x, spot size 3.0, working distance of 23.9 mm. Image shows 3-D structure of ZnO nanowires. (b) Top down view of ZnO nanowire, approximately 1 μ m in diameter. SEM Image taken at accelerating voltage of 30 kV, magnification 25,600x, spot size 3.0, working distance of 7.9 mm. Image shows ridge along length of wire, common in the structures examined.....	31
Figure 19.	Screenshot from NWS Ver1760 software. Under the SPM control tab, the LockIn, Stepper Motor Control, Setpoint, and Read Chanel	

	functions are located. Indications for Scan, Step Motor, and In Contact are located in the upper right.....	32
Figure 20.	Sweep graph of amplitude versus frequency. The sweep signal is set to magnitude and the feedback mode is Phase feedback. The Total gain and Oscillation Out 1 settings have been adjusted to achieve a maximum amplitude of 8V. In this case, the frequency is set at 35.44 kHz. The Autophase and Set Frequency buttons can also be seen on this screen.....	34
Figure 21.	Sweep graph of amplitude versus frequency. The sweep signal is set to Squared and the feedback mode is Phase Feedback. The cursor is moved to where the resonance curve crosses the x-axis. The frequency, in this case, is set at 35.44 kHz.	35
Figure 22.	Scan Window. The scan directions of the raster scan, horizontal and vertical, are selected from this tab. The user can also select the size of the fast and slow axis, the number of points, and the time per point, for the scan window. The start button initiates the scan with the selections made.....	36
Figure 23.	Typical Feedback Gain settings on the SPM Controller. The Low Pass filter and Integrator settings are rotated fully clockwise to the maximum value. The Differential setting is rotated fully counter-clockwise to the minimum value. The Proportional setting is rotated clock-wise to the “10 o’clock” position.	37
Figure 24.	Relative position of electron beam and probe tip on a nanowire at ~20000x. The electron beam is placed on the nanowire in spot mode. The probe tip is away from the electron beam and performing a raster scan of the nanowire featured. Some diffusion length data are lost by starting the probe tip far away from the cathodoluminescence generation site.	40
Figure 25.	Relative position of electron beam and probe tip on a nanowire at ~20000x. The electron beam is placed on the nanowire in spot mode. The probe tip is away from the electron beam and performing a raster scan of the nanowire featured. By placing the probe tip close to the electron beam, the chances of incidental contact increase. The risk increases that photons would be generated in the probe tip vice the nanowire being investigated and bias diffusion length results. This phenomenon would be more pronounced when measuring a low luminescent material.	41
Figure 26.	NSOM probe tip with 300 nm aperture at 13000x. The scan window is composed of the Si substrate without any nanowires. The overlay shows the length measurement (green) used to place the electron beam to perform the control experiment raster scan. The fixed electron beam and the path of the probe’s downward raster scan are shown (yellow) for illustration.....	42
Figure 27.	NSOM profile data for five control experiment trials. Intensity, in arbitrary units, is plotted on the vertical axis. Distance, in microns,	

	is plotted on the horizontal axis. The intensity increases as the raster scan progresses and the electron beam s closer to the tip of the probe. Once the probe tip scan path progresses beyond the fixed electron beam position the intensity drops precipitously. Outside of approximately 1 μ m from the electron beam, the NSOM signal has decayed to zero.	43
Figure 28.	Data from Figure 27, focusing on the region between zero and 2.5 μ m.	44
Figure 29.	Cathodoluminescence for the silicon based NSOM/AFM probe tip. Intensity, in arbitrary units, is plotted on the vertical axis. Wavelength, in nanometers, is plotted on the horizontal axis.	45
Figure 30.	Filter performance for 400FL07 short-pass filter offered by Andover Corporation. Transmission percentage is on the vertical axis. Wavelength, in nanometers, is on the horizontal axis. The 50% transmission point is 400 nm.	46
Figure 31.	Filter performance for 450FL07 short-pass filter offered by Andover Corporation. Transmission percentage is on the vertical axis. Wavelength, in nanometers, is on the horizontal axis. The 50% transmission point is 450 nm.	47
Figure 32.	Combined transmission percentage with 400 nm and 450 nm short-wave pass filters (blue) and the cathodoluminescence (CL) spectrum for NSOM/AFM probe tip (green), calculated from data provided for each filter by the manufacturer. The vertical axis is transmission percentage for the filters and the CL intensity of the probe tip. The horizontal axis is the wavelength in nanometers.	48
Figure 33.	The dual filter arrangement. Light travels from the NSOM via fiber optic wire and is then filtered by the 450 nm short-pass filter and then the 400 nm short-pass filter before entering the photomultiplier tube (PMT).	49
Figure 34.	Control experiment conducted to verify performance of filters. Intensity, in arbitrary units, is plotted on the vertical axis. Distance, in microns, is plotted on the horizontal axis. The signal generated in the first two microns of the scan, where the probe tip contribution is believed to be is reduced by the use of the filters. The 400 nm filter alone reduced the signal to one-third the original value. The use of both filters reduced the original signal an order of magnitude.	50
Figure 35.	The effect of adding both 400 nm and 450 nm short-pass filters to the path to the PMT for the CL of a ZnO nanowire. Intensity, in arbitrary units, is plotted on the vertical axis. Distance, in nanometers, is plotted on the horizontal axis. The signal is reduced by approximately ~30%.	51
Figure 36.	(a) Intensity plot of NSOM data. Brighter and more dense color indicates higher light intensity. A profile (green) is taken along the axis of the wire.(b) Intensity plot of AFM height data. Brighter colors indicate a higher elevation of the nanowire topography.	54

Figure 37.	The profile generated from NSOM intensity data. The graph axes are intensity as function of distance.....	55
Figure 38.	3D NSOM data showing the decrease of the light intensity as the probe scans away from the generation site along the wire axis	56
Figure 39.	Diffusion length as a function of diameter. Error bars are as indicated in Table 1.	57
Figure 40.	Diffusion length as a function of nanowire diameter. Diffusion length was measured by a near field photocurrent microscopy technique. From [30].....	58
Figure 41.	AFM and NSOM data on the NWS1760 software. The top portion of the readout is real time data. The AFM and NSOM are independent but graph on top of each, indicating a common spatial component. This is expected as the light is generated within the wire. The lower two are a waterfall display of the AFM and NSOM data with the newest data at the top. In both views, the AFM data is in red and the NSOM data is in blue. Waveguiding is shown as the NSOM light intensity data increases at the end of nanowire, after the initial surface diffusion. Some light from cathodoluminescence is transmitted internally through the ZnO nanowire.....	60
Figure 42.	Normalized intensity (arbitrary units) as a function of distance in microns. The intensity was taken from a fast axis profile across the brightest portion of the waveguided signal. This figure shows graphically that the amount of spreading appears to be invariant with the spot size (probe current).....	62
Figure 43.	The NSOM data with the 3D version beneath each respective 2D version. Image (a) and (b) are for spot size 4, (c) and (d) for spot size 5, (e) and (f) for spot size 6, (g) and (h) are for spot size 7.	63
Figure 44.	Maximum intensity (arbitrary units) as a function of spot size. Intensity is plotted on vertical axis while spot size is on the horizontal axis. The intensity increases with spot size but is non-linear, particularly at higher spots sizes.....	64
Figure 45.	Maximum intensity (arbitrary units) as a function of the current. The intensity is on the vertical axis in arbitrary units. The current, in pA, is on a log-scale horizontal axis. The intensity increases with but is nonlinear, particularly at higher currents.....	64
Figure 46.	6x6 μm NSOM scans of waveguided intensity as a function of distance, D, from the generation site. The limit, to first order, appears to be between 25-30 μm	66
Figure 47.	Maximum intensity waveguided as a function of distance between electron beam and end of nanowire.	67
Figure 48.	Plot of absorption coefficient (cm^{-1}) versus photon energy (eV) for ZnO thin films (red) and the ZnO nanowire estimation (blue). After [34].	68

Figure 49. Plot of natural log of the absorption coefficient (cm^{-1}) versus photon energy (eV) for ZnO thin films (red) and the ZnO nanowire estimation (blue). After [34]. 68

LIST OF TABLES

Table 1.	ZnO nanowire diffusion length as a function of wire diameter.	56
Table 2.	The Full Width Half Maximum (FWHM) as a function of spot size.....	62

THIS PAGE INTENTIONALLY LEFT BLANK

LIST OF ACRONYMS AND ABBREVIATIONS

AFM	Atomic Force Microscope
CL	Cathodoluminescence
DT	Data Transition
FWHM	Full Width at Half Maximum
E_g	Bandgap
eV	Electron Volts
NSOM	Near Field Scanning Optical Microscope
PMT	Photomultiplier Tube
PVD	Physical Vapor Deposition
SEM	Scanning Electron Microscope
SPM	Scanning Probe Microscope
UV	Ultraviolet
VLS	Vapor-Liquid-Solid
ZnO	Zinc Oxide

THIS PAGE INTENTIONALLY LEFT BLANK

ACKNOWLEDGMENTS

I am grateful for my wife, Lisa, my closest friend. Her support, encouragement, and attentiveness made the entire thesis process much more manageable and enjoyable. I would like to thank Dr. Nancy Haegel for her enduring patience as well as the leadership and motivation she provides to each of her students.

Dr. Zhong Lin Wang and Dr. Yanguang Wei of the Georgia Institute of Technology provided the ZnO nanostructures. Funding was provided by the Defense Advanced Research Projects Agency (DARPA) and the National Science Foundation DMR 0804527.

THIS PAGE INTENTIONALLY LEFT BLANK

I. INTRODUCTION

A. THESIS SCOPE

The purpose of this thesis is to advance the novel method of studying diffusion length and waveguiding phenomenon in Zinc Oxide (ZnO) nanowires by spatially mapping cathodoluminescence with near field microscopy. The novel method involves utilizing a combined near field scanning optical microscope (NSOM) and atomic force microscope (AFM) probe inside the chamber of a scanning electron microscope (SEM). This thesis improves the previous work by using a higher resolution SEM, with much smaller beam diameter, for more precise electron beam placement for generating cathodoluminescence. The thesis also improves upon the method by introducing filters that reduce the signal contribution from the inherent luminescence of the AFM/NSOM probe. Using the improved methods, this thesis seeks to find the variation in diffusion length as a function of nanowire diameter/thickness. In investigating the waveguiding phenomenon, this thesis worked to measure the amount of spreading as a function of spot size (carrier generation rate). This thesis also makes a first attempt to measure the waveguiding limit and estimates the absorption coefficient for luminescence in ZnO nanowires.

B. BACKGROUND

1. Trends in Electronics

Gordon E. Moore, co-founder of Intel, described the advancement in transistor technology in a 1965 paper [1]. In the paper, Moore noted that the number of components in integrated circuits had doubled every year since the invention of the integrated circuit and predicted that this trend would continue.

This trend, now referred to Moore's law, has proved uncannily accurate. The IBM 1401, a variable word length decimal computer, debuted in 1959. It filled an entire room and weighed thousands of pounds. Adjusted for inflation, it would cost about \$1.5 million. The 1401 could perform 4000 calculations per

second, and was considered state of the art in its day. Today, the average mobile phone contains a microchip about the size of a thumbnail, considerably more affordable, and performs roughly 1 billion calculations per second [2]. The capabilities of many digital electronic devices are strongly linked to Moore's law: processing speed, memory capacity, battery technology, and size of sensors [3]. Moore's law and similar predictions are expected to continue to hold until physical and practical limits are met [3]. In order to propel electronic devices even to these boundaries, a more complete understanding of materials on increasingly smaller scales is required. Transport parameters, such as minority carrier diffusion lengths and lifetimes, for both holes and electrons, are critical to this understanding. Minority carrier diffusion lengths, correlated with other material properties, assist in the modeling and development of electronic devices, including the performance of switches and other bipolar devices, as well as predicting the range of suitable thicknesses for structures [4].

2. Nanowires

A nanostructure is a material in which at least one of its dimensions is on the nanometer (1×10^{-9} m) scale. The focus of this thesis is on semiconductor nanowires in particular, which have a width and thickness on the order of nanometers, but have lengths several hundred microns or greater. One-dimensional nanostructures have received increasing attention by academia and industry due to their characteristics. Nanowires have unique physical, chemical, magnetic, electric, optic, and thermoelectric properties as compared to their bulk parents [5]. Nanowires may also introduce interesting quantum effects such as confinement.

Advancements in nanotechnology have improved many consumer products, from sunscreen to scratch-resistant coatings. However, some of the perhaps more interesting applications have yet to be fully developed and lie in the area of electronics and photonics. These structures show great potential in use for the next generation nanoelectronic devices [6]. The one-dimensional

nanostructures have been demonstrated as active components or interconnects in photodetectors [7], single- electron transistors [8], electron emitters [9], field-effect transistors (FETs) [10], light-emitting diodes (LEDs) [11], biological and chemical sensors [12], and ultraviolet nanolasers [13]. Being able to create entire devices and systems on this scale could lead to lighter, more mobile, and more efficient integrated electronics.

The modern military also stands to benefit from the development of such nanoelectronics, just as it benefited from the silicon electronics revolution that transformed communications, computing, and imaging.

C. DEFENSE RELEVANCE

Technology changes warfare. From RADAR and SONAR, rocket propulsion, and the atomic bomb in World War II to the high tech drones, satellite imagery, surgically precise weapons, and advanced missile defense of today, technology has changed the nature of combat. Virtually every fighting platform, air, sea, land, space, and cyberspace has benefited from advances in technology, whether developed specifically for military applications or adopted from private sector commercial innovation.

Today's U.S. soldier can be equipped with a helmet-mounted GPS navigation receiver, a small wireless intrasquad voice and data communications system, and a wearable computer linked to an intrasquad LAN. A soldier's helmet can include thermal and night-vision sensors. A soldier can access and navigate computers and digital maps using his movement and a track pad mounted beneath his uniform [14]. Team members can communicate seamlessly and relay information back to headquarters in real-time for better situational awareness and decision-making. The fact that technology has progressed and gotten smaller, more energy efficient, and affordable, allows soldiers today to have many of the tactical advantages they enjoy. However, there is room for still more improvement in the size and weight of equipment.

Combat soldiers in the field have to prioritize size and weight in the gear they are detailed. According to the Army field manual for foot marches, a fighting load is everything worn or carried except a rucksack and should be held to less than 48 pounds. A march load should not exceed 72 pounds. In the worst-case scenario, an emergency approach march load can raise the total weight to between 120 and 150 pounds [15]. A recent study of fighters in Afghanistan placed the average rifleman's fighting load at 63 pounds [16]. This meant that soldiers were carrying about 36% of their bodyweight without a rucksack. The data report that march loads are an average of 55% of the soldier's body weight, and emergency approach march loads are about 71% of average body weight [16].

For survival and mission success, the right balance and compromise between weapons, sensors, communications, survival equipment, food, and water, must be met. Weapons, ammunition, and food are not practical areas for appreciable reductions in size and weight. Reducing the size and weight of sensors, communications, and other systems that involve electronics and electro-optics, while maintaining or improving capability, is a priority for today's military. Nanoelectronics could serve to reduce those size and weight demands on soldiers in the field, leading to a more mobile and dynamic fighting force. In addition, new materials and devices could lead to new applications. Nanowires have the potential to make ultraviolet (UV) and blue-green lasers and sensors low cost and widely deployed, with applications to include missile warning sensors on aircraft, sniper location, underwater communications and chemical-biological sensing systems. Nanotechnology has the potential to expand this range of applications when the devices and materials can be produced in volume.

D. MICROSCOPE CONCEPTS

1. Near-Field Scanning Optical Microscopy

Near-field scanning optical microscopy (NSOM) is an advanced technology that allows for imaging with sub-micron resolution. The conventional far-field resolution is limited by diffraction at the aperture. The observation of sub-wavelength structures with microscopes is inhibited due to what is known as the Abbe diffraction limit [17]. The basic principle is that light of wavelength λ will converge on a spot with radius d ,

$$d = \frac{\lambda}{2n(\sin \theta)} \quad (1)$$

where n is the index of refraction for the medium in which light travels, and θ is the angle of incidence of the light. The denominator is generally referred to as the numerical aperture. In modern optics, the numerical aperture can be about 1.4 in air [17]. Therefore, the diffraction limit is roughly half of the wavelength of the observed light. The spatial resolution would be compromised in the far field, as the light spreads. This resolution limit would be significant in measuring structures on the nanometer scale, where the dimensions are comparable to the wavelength of the visible and ultraviolet light collected. For example, the wavelength of light emitted from a ZnO nanowire is on the order of ~ 380 nm, while nanowires can be fabricated with diameters as low as ~ 20 nm and diffusion lengths that characterize transport can be less than 100 nm [17].

The diffraction limit is only valid for the far-field. Near-field, less than a distance of $\lambda/3$ from the surface of the structure, can allow for imaging that is not affected by the Abbe diffraction limit. The NSOM can collect photons with high spatial resolutions due to its ability to operate so closely to the surface of the sample.

The idea of overcoming the diffraction limitation by use of the near-field was first proposed by E.H. Synge in 1928 [17]. He also pointed out the difficulty of maintaining a sample in the near-field zone due to the surface roughness inherent in most materials.

Detecting the microscopic effective field near the surface of the sample places certain restraints on the probe tip. The probe tip must have a dimension on the same order as the object under investigation. Moreover, the probe tip must be placed near the object, typically within a few nanometers, and be maintained at this distance from the surface while scanning and imaging. Despite the theoretical claims made by Synge, it was not until the techniques developed in scanning tunneling microscopes and atomic force microscopes (AFM) were developed, that the potential of NSOM could be realized. A feedback mechanism, used typically in an AFM, is integrated to maintain the NSOM probe tip in the near field. Within the near field regime, the spatial resolution is dependent on the probe aperture size and not the wavelength of light [17]. A tradeoff occurs between higher spatial resolution and lowering transmission efficiency of signal, as the NSOM tip aperture decreases.

NSOM technology can operate in different modes. The primary modes are transmission, reflection, illumination, and collection mode [18]. In transmission mode, a sample is illuminated through the probe, and the light passing through the sample is collected and detected with a separate detector. Reflection mode has the sample illuminated through the probe and the light reflected from the sample surface is collected and detected. Illumination mode uses the probe for both illumination of the sample and collection of the reflected signal. In collection mode imaging, the sample is generally illuminated by an external source and the probe is used to collect the light from the sample surface. The NSOM featured in this experimental setup is operating in collection mode. Unique to these experiments, the photons are generated by cathodoluminescence by a source external to the NSOM (the Scanning Electron Microscope). The light is coupled into a tapered optical fiber via the sub-

wavelength aperture and then propagates through the fiber to the detector. The optical fiber wire is coated with a metal, typically aluminum.

2. Atomic Force Microscopy

Atomic force microscopy is a very high-resolution scanning probe microscopy. It was developed using piezoelectric scanning, probe tip, and sophisticated electronics and vibration control concepts furthered by the 1986 Nobel Prize winning scanning tunneling microscope. The first commercially available atomic force microscope (AFM) was made in 1989, following the scanning tunneling microscope [19]. The AFM is now a common tool used to measure, image, and manipulate material at the nanoscale. A mechanical probe is used to detect the surface topography variations of a sample. A cantilevered sharp tip is positioned and brought close to the surface and resonated in small accurate oscillations by an attached tuning fork. The probe tip and sample can be moved in three-dimensional space by a piezoelectric system. Because the technology is based on the physical feedback system and not light, the resolution is limited by the width or radius of the tip and the spring constant of the cantilever, rather than diffraction. The tip of the cantilever is scanned <10 nm above the sample. Van der Waals and shear forces are detected from the surface and a feedback system is employed to maintain a constant force, by adjusting the tip-to-sample distance. The feedback system senses the forces from the sources, compares it to a user defined setpoint, and adjusts the distance to compensate.

3. Combined AFM/NSOM Probe Tip

The probe tip selected in this work is an extended cantilevered NSOM optical fiber probe with a tapered tip. The tapered tip was selected because a straight tip would require a shear force feedback system and not allow for normal force feedback. Normal force feedback is based on well-defined interactions and understood better than shear force [20]. Additionally, shear force imaging may introduce serious artifacts in images. Figure 1 shows a typical AFM/NSOM

probe. A tapered fiber optic wire is glued to the AFM tuning fork. The fiber optic wire is cantilevered and contains an optical aperture at its end.

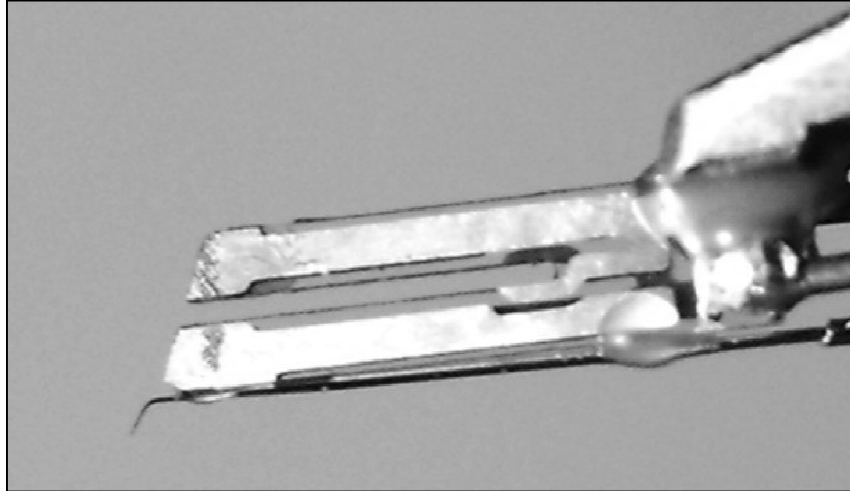


Figure 1. Combined AFM/NSOM probe tip. Tip includes a cantilevered tapered fiber optic wire with aperture at one end for collecting light. This is the NSOM portion of the tip and is glued to the tuning fork, which makes up the AFM portion of the tip. The AFM portion of the tip is responsible for vibrating at resonant frequency, sensing the topography of the sample, and using the feedback mechanism to maintain the probe close to the surface sample. The NSOM collects the light from the sample surface and transmits the light along the fiber optic wire. From [20] .

As one system, the probe is coupled with the surface of the sample, and is scanned across the surface of the sample. This process is called a raster scan. In raster scanning, a line-by-line scan progresses across the surface in a rectangular pattern. The sample or the probe is moved relative to the other via piezoelectric drivers. The pattern is then transmitted as an integrated image of the scanned surface.

E. CATHODOLUMINESCENCE

Cathodoluminescence (CL) is an optoelectronic phenomenon in which electrons are used to impact a luminescent material such that visible, UV, or IR

light is emitted [21]. The luminescent material is typically a direct bandgap semiconductor. The electron beam is generated by, in this case, a scanning electron microscope (SEM).

Figure 2 shows a simplification of the process that occurs as electrons are incident on the semiconductor sample. The accelerated electrons bombard the sample and initiate a series of interactions. A percentage of these interactions produce electron/hole pairs that recombine to produce photons with an energy equal to the bandgap of semiconductor. The imaging of the photons is the principle focus of this thesis.

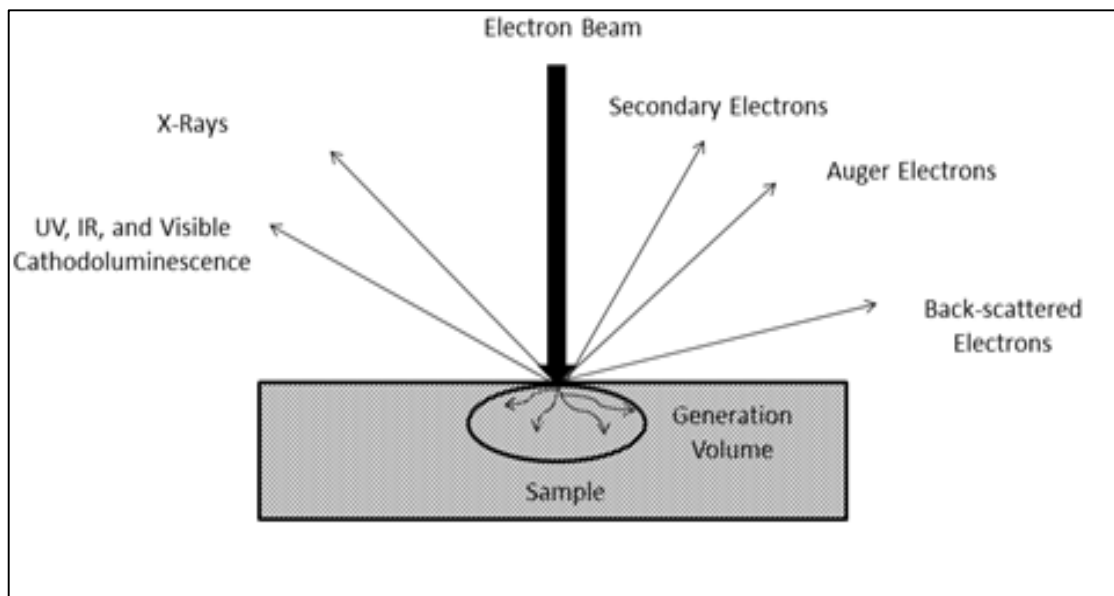


Figure 2. An electron beam incident on a semiconductor sample. Many interactions are possible and do occur. The principle focus of this thesis is on cathodoluminescence, where the electrons excite free electrons and holes. Those electrons and holes then de-excite and give off energy in the form of a photon. After [21].

Equation 2 relates the bandgap energy, E_g , with the wavelength of the photon generated by cathodoluminescence, λ ,

$$E_g = \frac{hc}{\lambda} \quad (2)$$

where h is Planck's constant and c is the speed of light. The numerator, hc , is approximately 1240 nm-eV.

F. BASIC SEMICONDUCTOR PRINCIPLES

1. Band Structure

A semiconductor is a material with an electrical conductivity that lies between conductors and insulators [22]. In classic crystalline semiconductors, electrons can only have certain ranges of energy or bands. These ranges of energy represent many closely spaced molecular orbitals with discrete quantum states. The lower energy band is referred to as the valence band. The upper, mostly unoccupied, band is referred to as the conduction band. When electrons are excited to the conduction band, they can then contribute to current flow. The excited electron that has been elevated to the conduction band leaves behind a hole in the valence band. Another electron can then fill that hole. In this way, holes can be seen as a moving positive charge, the absence of a negatively charged electron, and contribute to the electrical conductivity of the material.

The forbidden band gap, that contains no allowed electron energy levels, separates the valence band and conduction band. The size of the forbidden band gap or band gap (E_g), is the distinguishing characteristic of semiconductors, compared to other materials. In metals, there is no band gap. Therefore, the valence and conduction bands overlap, allowing for free transition of electrons. This is what leads to the high electrical conductivity of metals at all temperatures. Conversely, insulators have relatively large band gaps. Very few electrons will be found in the conduction band, leading to a correspondingly low electrical conductivity. The band gap for semiconductors lies between insulators and

metals and is on the order of a few electron volts (eV). Figure 3 shows the relationship between metals, semiconductors, and insulators, with respect to the bandgap (E_g).

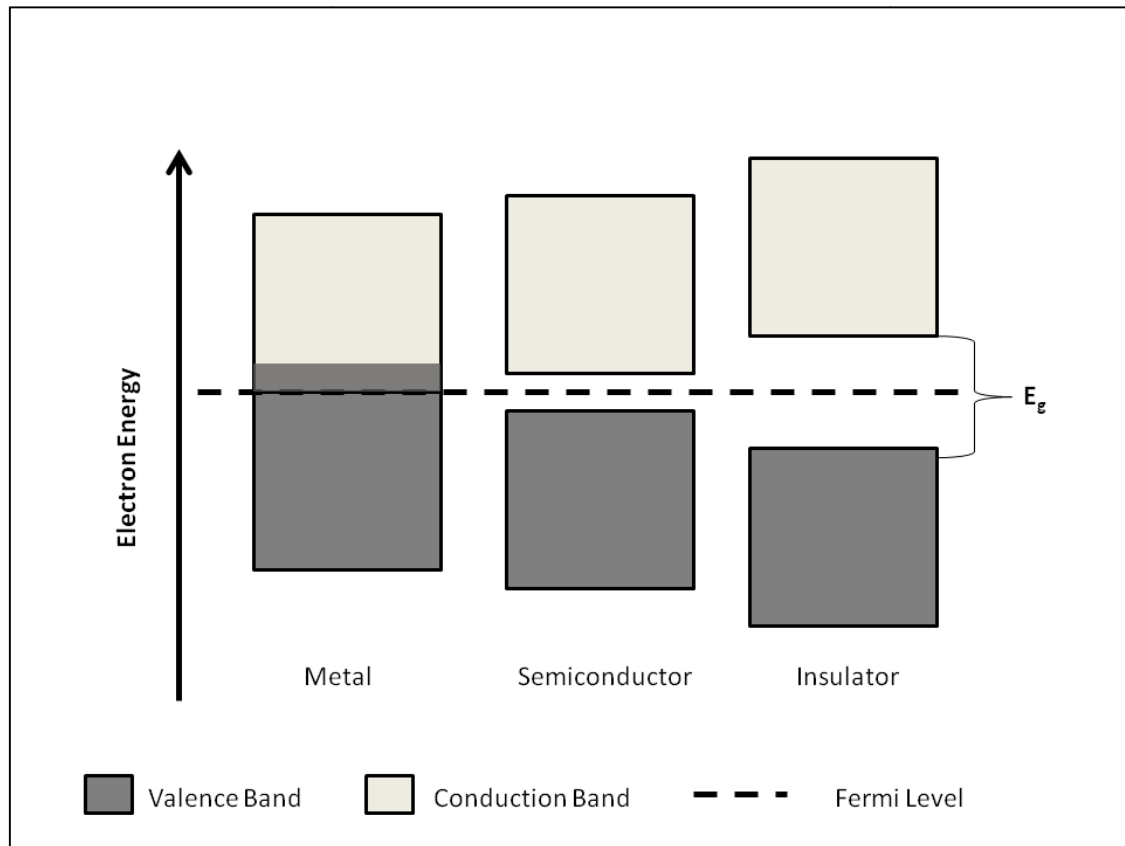


Figure 3. The conduction band and valence band, separated by the bandgap. Note that metals do not have a forbidden region or bandgap; the valence band and conduction band overlap. The insulator has the largest band gap. The semiconductor has a smaller bandgap than the insulator. The Fermi level is located approximately half way through the forbidden zone. After [23].

2. Direct and Indirect Bandgaps

A direct bandgap semiconductor is one in which the momentum is the same for the electrons at the bottom of the conduction band and the holes at the top of the valence band. An indirect bandgap material is one in which the momentum of the electron and hole, at the conduction band minimum and

valence band maximum, are not the same [24]. Radiative recombination, the process of releasing a photon as the electron de-excites and annihilates the hole, is possible when the momentum is matched between the conduction and valence bands. The emitted photon has negligible momentum. An energy and momentum plot shows that when the momentum is shifted between the conduction band and valence band, momentum is not conserved. The photon cannot carry the momentum of the crystal lattice. A crystal defect, a recombination center, or a phonon is needed to conserve momentum. A phonon is a particle that carries energy associated with a compressional wave, such as the vibration of a crystal lattice. In this case, the phonon also has momentum equal to the difference in the conduction band and valence band momentum. The necessity for the production of a phonon in indirect bandgap materials in order for radiative recombination to take place lowers the rate and probability of such occurrences. Radiative recombination is the means through which cathodoluminescence occurs. The luminescence of a material depends on many factors including purity, defect state, and the type of material. In general, however, a direct band gap semiconductor will luminesce more strongly than an indirect band gap semiconductor. Figure 4 shows this phenomenon as described. The material studied here, Zinc Oxide (ZnO), is a direct bandgap material.

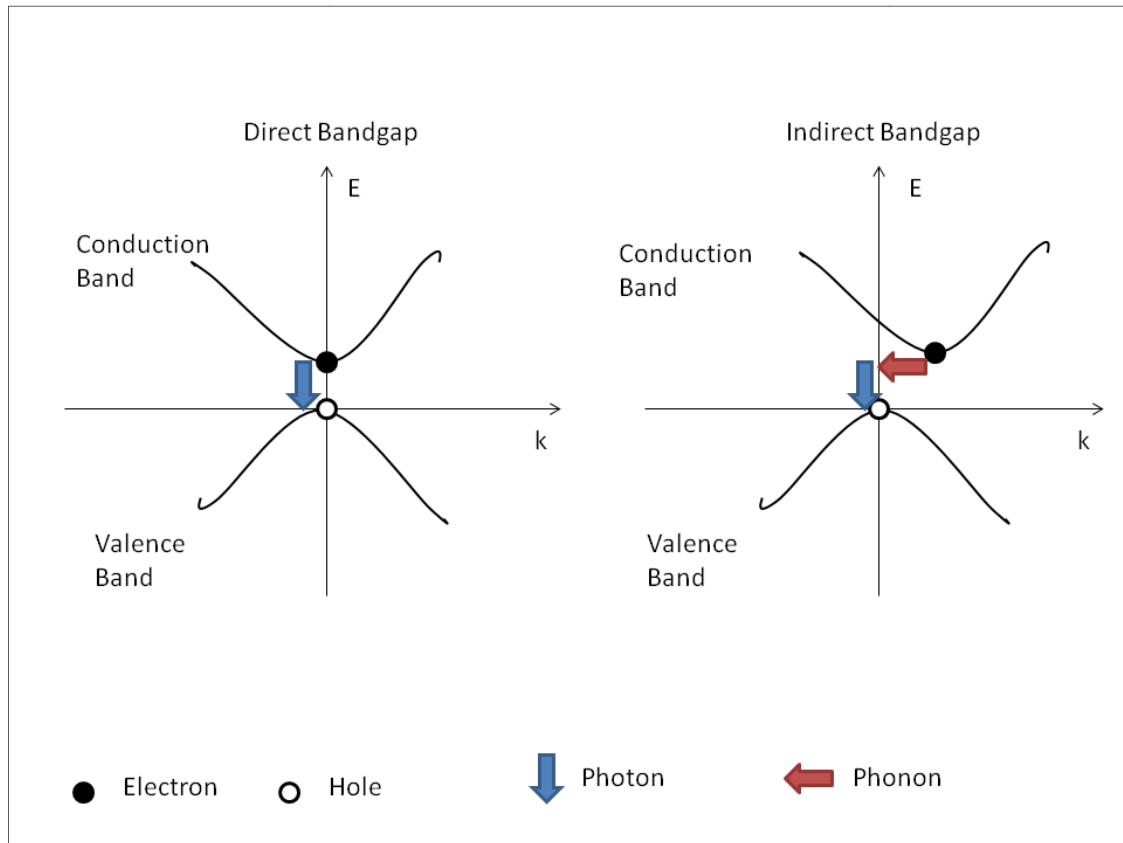


Figure 4. Direct and indirect bandgap semiconductor material shown on an energy (E) versus momentum (k) graph. The conduction and valence bands are separated by the bandgap. For the indirect bandgap material, the momentums are not equal for the preferred transition of the electron. In order for momentum to be conserved, a phonon has to be released in addition to the photon. The direct bandgap electron de-excitation does not require a phonon as the momentums are equal. The requirement of the additional particle makes radiative capture less likely in indirect bandgap materials. Therefore, a direct bandgap material tends to luminesce more by such techniques as cathodoluminescence. After [24].

G. NANOWIRE GROWTH PROCESS

There are various methods used by laboratories to synthesize nanowires including suspension, Vapor-Liquid-Solid (VLS), and electrochemical or vapor deposition. The sample examined in this thesis uses a physical vapor deposition method referred to as thermal evaporation. The thermal evaporation technique is

a simple process, in principle, that involves vaporizing a source material (condensed or powder) under high temperature and then condensing the products under specified conditions to promote desired characteristics [25]. The process is normally undergone in a tube furnace. A carrier gas is fed through the tube by a rotary pump. The tube maintains a vacuum pressure. A source material is loaded and the entire system is sealed. The carrier gas passes over the source material and the temperature gradient. The carrier gas transports the source material vapor from the high temperature region to the low temperature region, where the growth products condense and are deposited onto a substrate. The high evaporation temperature can be as high as 1400 °C and the low temperature substrate can be as low as room temperature [25]. Figure 5 shows a simplified diagram of the apparatus.

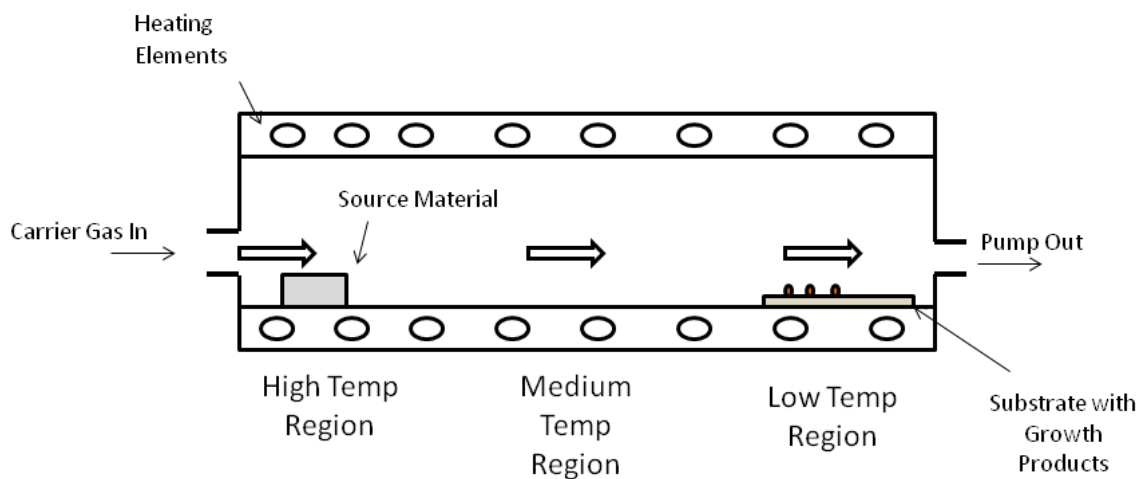


Figure 5. Thermal Evaporation process. The source material (e.g., bulk ZnO) is evaporated. A carrier gas transports the vapors to the low temperature region where it is condensed onto a substrate. After [25].

H. DIFFUSION LENGTH IN ONE DIMENSION

Electron transport in semiconductor nanowires can be modeled to first order as a one-dimensional phenomenon. The electric field is assumed to be negligibly small. Under time-invariant excitation, the steady state continuity equation results in a second order differential equation [26],

$$\frac{d^2 \Delta mc}{dx^2} = \frac{\Delta mc}{L_{mc}^2} \quad (3)$$

where Δmc is the change in the number of minority carriers and L_{mc} is called the diffusion length. The diffusion length is the characteristic distance the minority carrier, electron or hole, travels before recombination. The diffusion length is related to the carrier lifetime, the average time a carrier takes to recombine [26].

$$L_{mc} = \sqrt{D\tau} \quad (4)$$

where, D is the diffusion coefficient and τ is the carrier lifetime. The spatial solution to the differential equation, with appropriate boundary conditions, is an exponential decay. If the number of minority carriers recombining represents the intensity of light emitted, the following result is expected [26].

$$I(x) = I_0 \exp\left(-\frac{x}{L_D}\right) \quad (5)$$

where I is the light intensity and x is the distance away from the excitation point. There is no net emission in equilibrium. The diffusion length measured in this work represents the transport of non-equilibrium or excess carriers generated by cathodoluminescence.

I. WAVEGUIDES

A waveguide is an object that guides electromagnetic waves that lie in the optical spectrum. Optical waveguides include optical fiber like the type used to

transmit the NSOM data collected at the probe to the photomultiplier. Waveguides are important for the transmission of signals, including communications, over appreciable distances. Without appropriate waveguides, signals would be dispersed, distorted, or lost between devices. Nanowires are of interest for many of the optical applications because they are natural waveguides, confining the light to propagate along the wire axis by nature of the higher index of refraction compared to the surrounding air. This thesis uses the NSOM/AFM probe inside of an SEM to study diffusion and waveguiding phenomenon in ZnO nanowires. The next chapter discusses the general setup and methods employed for these experiments.

II. GENERAL EXPERIMENTAL SETUP AND METHDS

A. EXPERIMENTAL SETUP

1. Overview

The principal equipment consists of a combined NSOM and AFM apparatus (Nanonics Multiview 2000) mounted inside of a FEI Inspect F50 SEM chamber, along with associated interfaces, instrumentation, and control components. Figure 6 shows a basic block diagram illustrating the relational connections of each of the components of the Multiview 2000 system [27]. The purpose of the components will be described in this section.

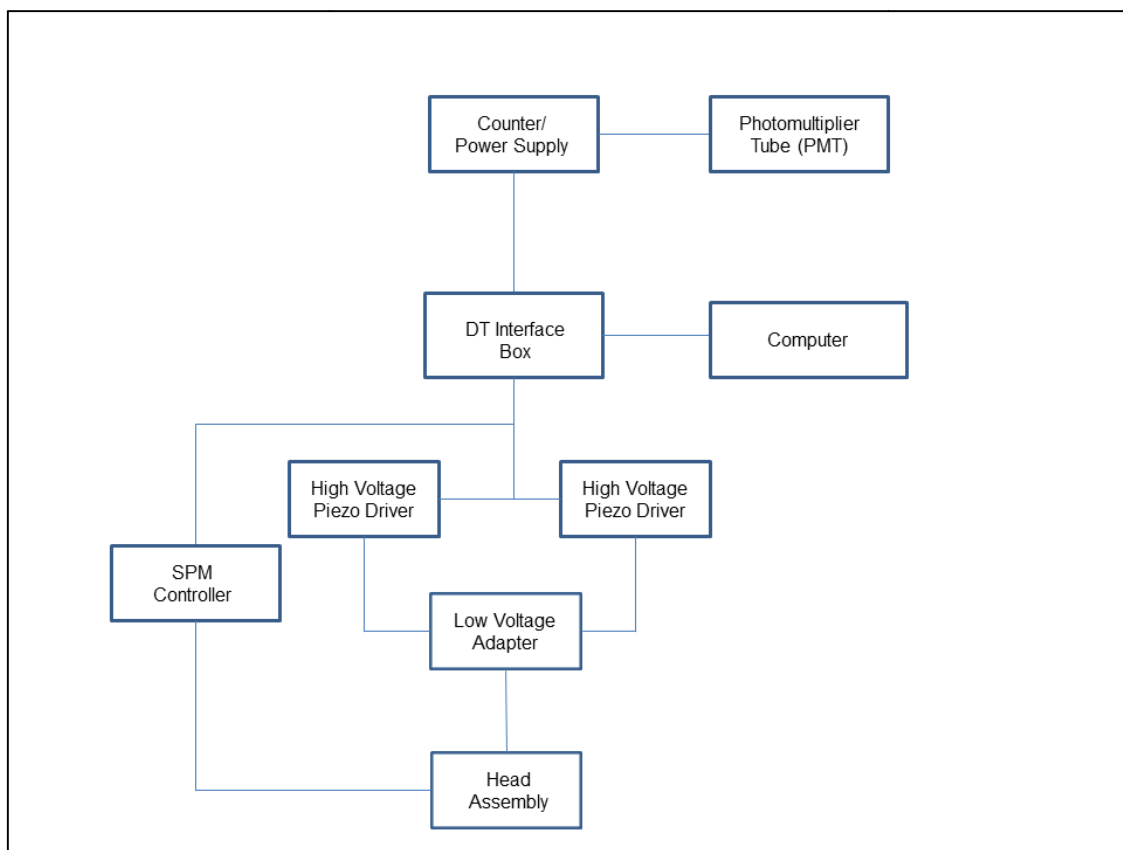


Figure 6. Basic functional block diagram of the control and instrumentation components for the Multiview 2000. After [27].

2. Head Assembly

The NSOM and AFM are combined in the head of the MultiView 2000. Figure 7 shows the head assembly of the MultiView 2000. The head consists of the lower sample scanner, upper scanner, and stepper motor. The upper scanner lies on top of the lower scanner and is responsible for the scanning and positioning of the attached probe in the x and y plane. The lower scanner is responsible for the scanning and positioning of the sample stage in the x and y plane. The lower scan may use inertial motion for course movements in the x and y plan. The inertial motion applies a voltage to the piezoelectric motors to move the sample. Due to the fork-based mount, the probe itself cannot be moved by inertial motion [27]. Both scanners can also make adjustments to the z axis position, via the feedback system or manually. Highly sensitive piezoelectric drivers accomplish the movements during automatic scans, manual positioning, and inertial motion [27].

The stepper motor (not shown) adjusts the height of the NSOM/AFM probe along the vertical or z-axis. The stepper motor is primarily used for the probe tip to approach and be retracted from the surface of the sample before and after scanning. As a convention, for this thesis, once the probe tip is in contact with the sample surface, only the feedback mechanism adjusts the z-axis position for the tip. The z-axis position was never adjusted manually. The adjustable screw to the right is used for course adjustment of the vertical position of the upper head relative to the lower head. The screw can then be tightened to prevent movement during scans.

The upper head can be rotated about the hinge that connects it to the lower head in order to provide clearance for placing, removing, or making physical adjustments to the sample. Figure 8 shows the Multiview 2000 head in this configuration. The sample is placed on an electrically isolated floating sample holder that lies on three piezoelectric pins. This minimal surface contact for the sample holder allows for the course inertial motion.

The upper and lower heads receive power and control from the four connectors shown in Figure 8. The electrical connections are for the top scanner, preamplifier, step motor, and the bottom scanner. The connectors also electrically ground the Multiview 2000 head to the SEM chamber. Additional grounds are achieved by a copper grounding wire and tape. The tip holder and tip on the upper scanner are grounded to the upper scanner. The sample is grounded to the lower scanner. The lower and upper scanners are in electrical contact and make a common ground with the SEM. The grounding has shown to reduce sample and probe tip charging effects in SEM imaging and electron beam positioning for higher spot sizes (SEM probe current). The grounding also reduced instances of the NSOM/AFM probe tips "crashing" into the sample during approaches. It appears that if the sample and probe tips do not have a common ground, then local fields can build up that will occasionally interfere with the feedback mechanism and cause the probe to "crash" into the surface.

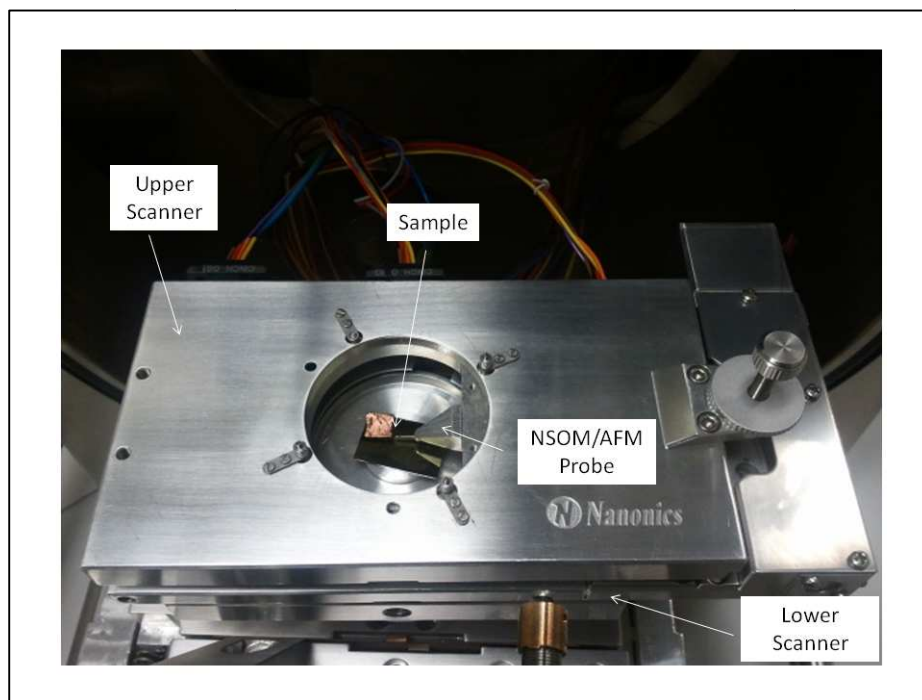


Figure 7. The Multiview 2000 head, developed by Nanonics Inc. This is the normal configuration for operation.

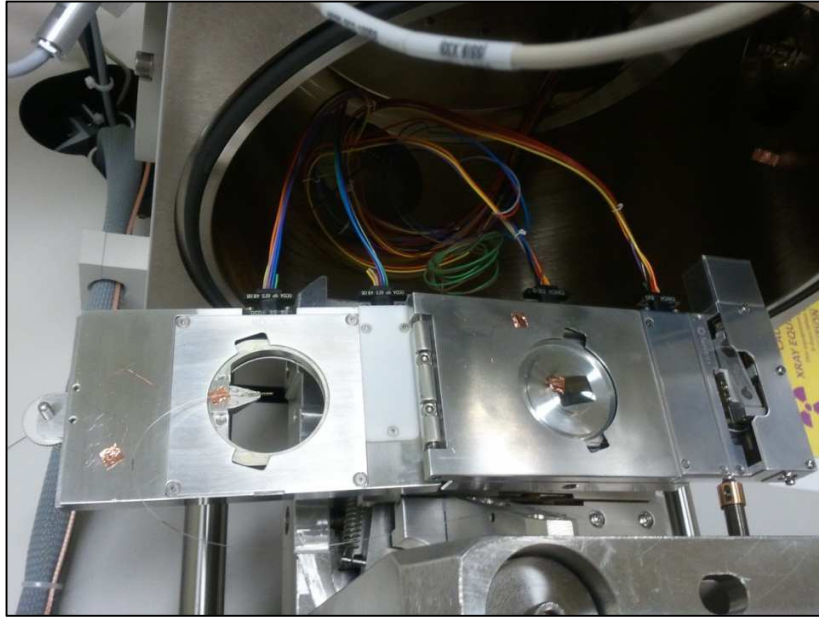


Figure 8. The Multiview 2000 head mounted in the chamber of the FEI Inspect F50 SEM. The AFM/NSOM probe is screwed into the upper scanner (left). The lower scanner (right) houses the sample. Copper wire and tape serve to ground the instruments. This view is with the upper scanner rotated about the hinge that connects the upper and lower scanners.

a. NSOM/AFM Probe

The NSOM/AFM probe is held in a metal holder with an electronic grid attached for implementing the fine control of the tip. The tuning fork is mounted beneath the holder by electrodes. A non-conductive glue guides and secures the tapered fiber optic wire of the NSOM to end of the AFM tuning fork. The fiber optic wire is selected for optimum ultraviolet (UV) transmission. Figure 9 shows the probe from two different aspects and the container for the probe.

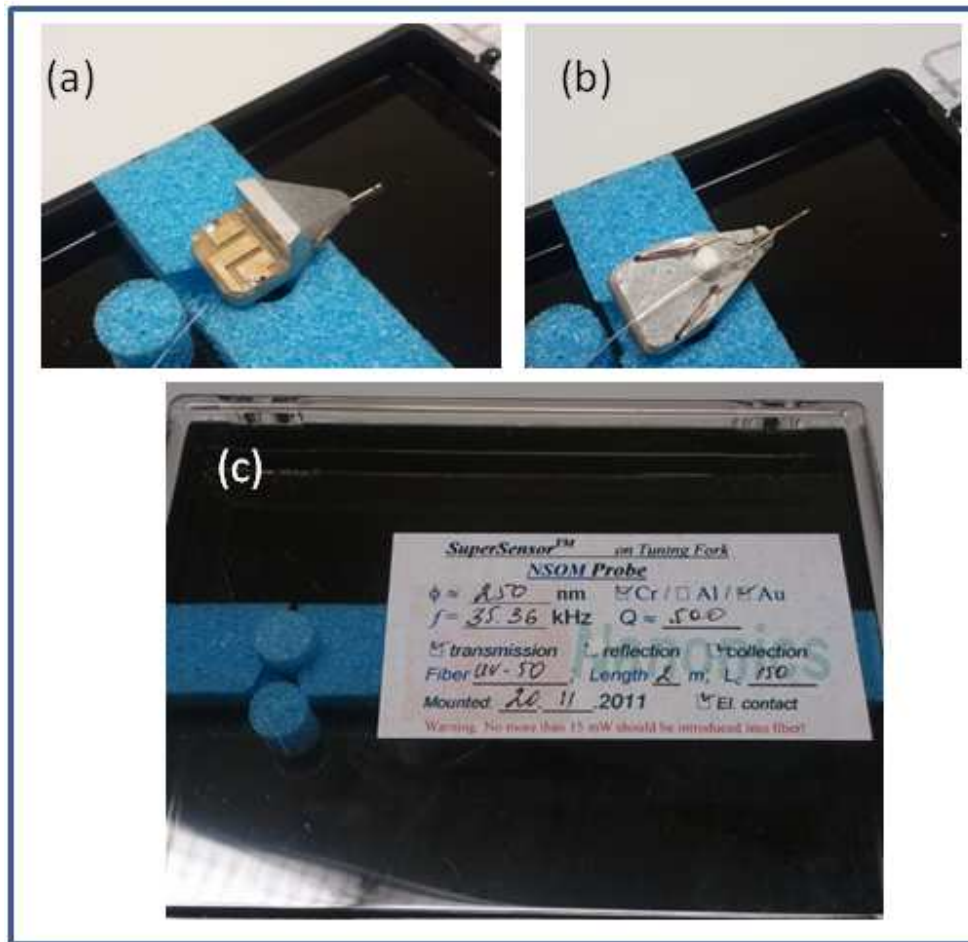


Figure 9. The AFM/NSOM probe. (a) The holder has an electrical grid attached to the back, which connects to the Multiview 2000 head assembly, and allows for the control of the tip. (b) On the underside of the holder, electrodes that connect the AFM tuning fork can be seen. A non-conductive glue is used to connect the tapered NSOM fiber optic wire to the end of the tuning fork. (c) The probe box contains important information about the probe such as the size of the aperture (ϕ), frequency (f), quality factor (Q), the mode (collection), and type of fiber (ultraviolet).

3. Computer

The Multiview 2000 has an independent computer. The NWS version 1760 software provides the interface for the control of the unit head.

4. Low Voltage Adaptor

Figure 10 shows the Low Voltage Adaptor. The Low Voltage Adaptor is used to select the scanners since the Multiview 2000 provides for option for independent tip and sample scanning and feedback [27]. The z-axis feedback is selected to “Upper” to ensure the tip, rather than the sample, is adjusted based on the feedback. The X-Y Scanning is positioned to "Upper" for scans since we need to move the tip on a fixed sample. However, the X-Y Scanning must be moved to "Lower" for moving the sample via inertial motion. This is performed with the tip retracted.



Figure 10. The Low Voltage Adapter is used to select either the upper or lower scanner for scanning and feedback adjustments.

5. Photomultiplier Tube

Figure 11 shows the photomultiplier tube (PMT) used to detect and amplify the light signal generated by cathodoluminescence. Photons gathered from the NSOM are transmitted, via the light guiding behavior of an attached fiber optic wire, to this photomultiplier tube [47]. The 400 nm and 450 nm short pass filters were added to the entry point of the PMT. The MP-983 photon counting module uses a low noise Bialkali photocathode to detect 185–650 nm light [28]. The sensing window is made of ultraviolet glass.



Figure 11. Photomultiplier tube fed by the fiber optic wire from the NSOM probe.

6. Counter and Power Supply

The counter and power supply module is shown in the upper right corner of Figure 12. The counter and power supply provides power (5V) for the photon detector [27]. The counter receives a TTL signal from detector and converts them to analog signals. The time constant sets the analog channel's smoothing filter. The count rate sets the frequency range in accordance with the maximum frequency of the output. Unless otherwise noted, the time constant was set to 2.0 ms and count rate was set to 1.0 kHz. These settings showed improved signal to noise ratios in the NSOM data. A digital readout provides an indication proportional to the number of counts being registered by the counter.



Figure 12. Upper Left Module: High Voltage Piezo Driver for the lower stage. Lower Left Module: SPM Controller. Upper Right Module: Counter and Power Supply. Lower Right Module: High Voltage Piezo Driver for the upper stage.

7. High Voltage Piezo Driver

The control boxes for the High Voltage Piezo Drivers are shown in Figure 12. There are two High Voltage Piezo Drivers to supply independent motion of the probe tip and sample. They are labeled upper and lower and connected to the appropriate scanner. The High Voltage Piezo Driver processes the signals from the SPM controller and supplies the high voltage signals necessary to move the piezoelectric crystals in the scanner [27]. The displays for each channel (axis) show the voltages that are applied at any given moment. The channels are referred to as X, Y, and Z.

There are three modes of operation: positioning, scan and offset, and scan and slope compensation. The Positioning Mode is used to move the tip relative to the sample (or vice versa) along the x, y, and z axis. The Scan and Offset Mode is used to manually move the tip relative to the sample (or vice versa) small distances during a scan. The Scan and Offset Mode is the mode

normally used when scanning. Power is generated to move the scanner on the “fast” axis and the scan also compensates for a continuous slope on the z-axis [25].

8. Scanning Probe Microscopy (SPM) Controller

The SPM Controller box contains a controller card, which controls the feedback of the scanner and a lock-in amplifier card for signal processing [27]. The feedback settings used to optimize feedback parameters are on this panel. The Integrator Gain defines how fast a correction is applied to the scanner, ie., the integration time for the Z direction. The Differential Gain adds a negative or positive signal to the Z correction voltage according to the gradient of the Error signal [25]. The Proportional Gain defines the magnitude of the correction signal. It amplifies the Error signal in order to get an appropriate correction signal. The feedback indicator is located here and informs the user when the probe tip is in contact with the sample.

9. Data Transition (DT) Interface Box

The DT Interface Box contains the electronic connections that provide an interface between the PC cards in the computer and the SPM Controller, scanner and photomultiplier tube [27].

10. Power Supply

The Power Supply, shown in Figure 13, is used to distribute power to each of the components. Specifically, the system provides low-voltage and high-voltage to the SPM Controller, DT Interface and High Voltage PiezoDriver [27].

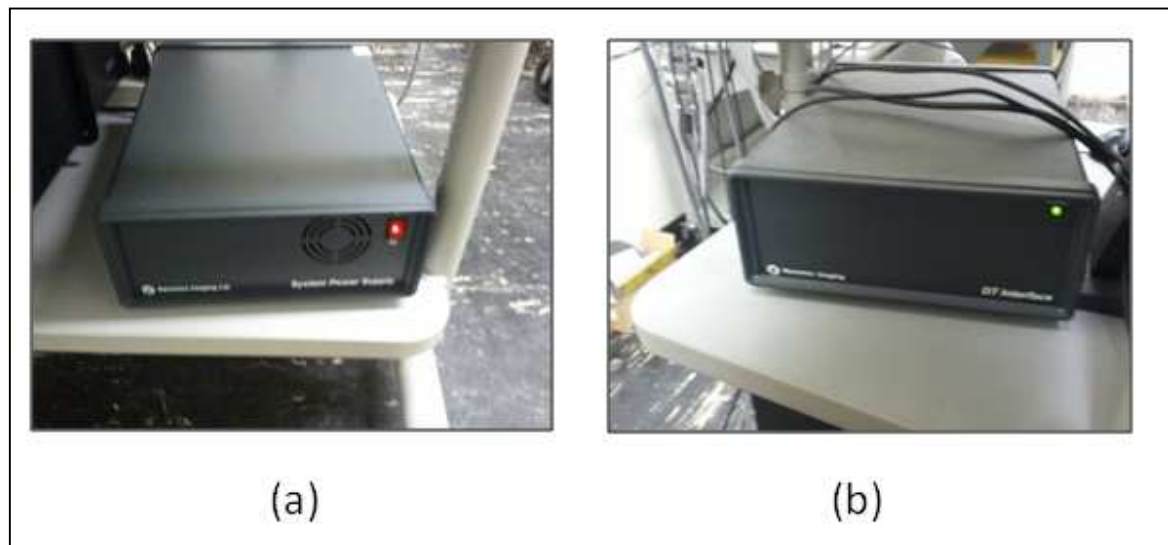


Figure 13. (a) System Power Supply and (b) The DT Interface.

11. The Scanning Electron Microscope (SEM)

The FEI Inspect F50 Scanning Electron Microscope provides high resolution secondary electron imaging over a wide range of magnifications. This gives the user situational awareness of the probe and the nanostructures on the sample as well as being the source of electrons for cathodoluminescence. Figure 14 shows the FEI Inspect 50.



Figure 14. FEI Inspect F50 Scanning Electron Microscope. The microscope is controlled by an independent computer.

The SEM is controlled separately by xT Microscope software loaded on a separate computer. The software provides the user interface for the experiments. Figure 15 shows the main user interface for the SEM. The SEM offers various operating modes and parameter variations. Significant experimental parameters include voltage and spot size (probe current). The accelerating voltage of the incident electrons can vary from 500 V to 30 kV. The spot size or probe current of the electron beam at the sample surface can vary from 1 to 7. Unless otherwise noted, a voltage of 20kV and a spot size of 3 were used in the experiments of this thesis.

The three modes of the SEM are full frame, line mode, and spot mode. The full frame mode provides a real-time image and is being continually updated based on the frame rate selected. In line mode, the SEM produces an electron beam along the axis of a line. The image is not refreshed in line mode. In spot mode, the electron beam is placed in very narrow diameter circle. The diameter of the spot varies with inversely with voltage and proportionally with spot size,

ranging from about 2 nm to 13 nm at a working distance of 10 mm. The beam diameter may differ at the actual working distances used, approximately 20 mm. For spot mode, a set of cross-hairs appear and can be moved by the user to direct the electron beam. The image is not refreshed in spot mode. Figure 15 shows the cross-hairs directing the electron beam for cathodoluminescence of a nanowire.

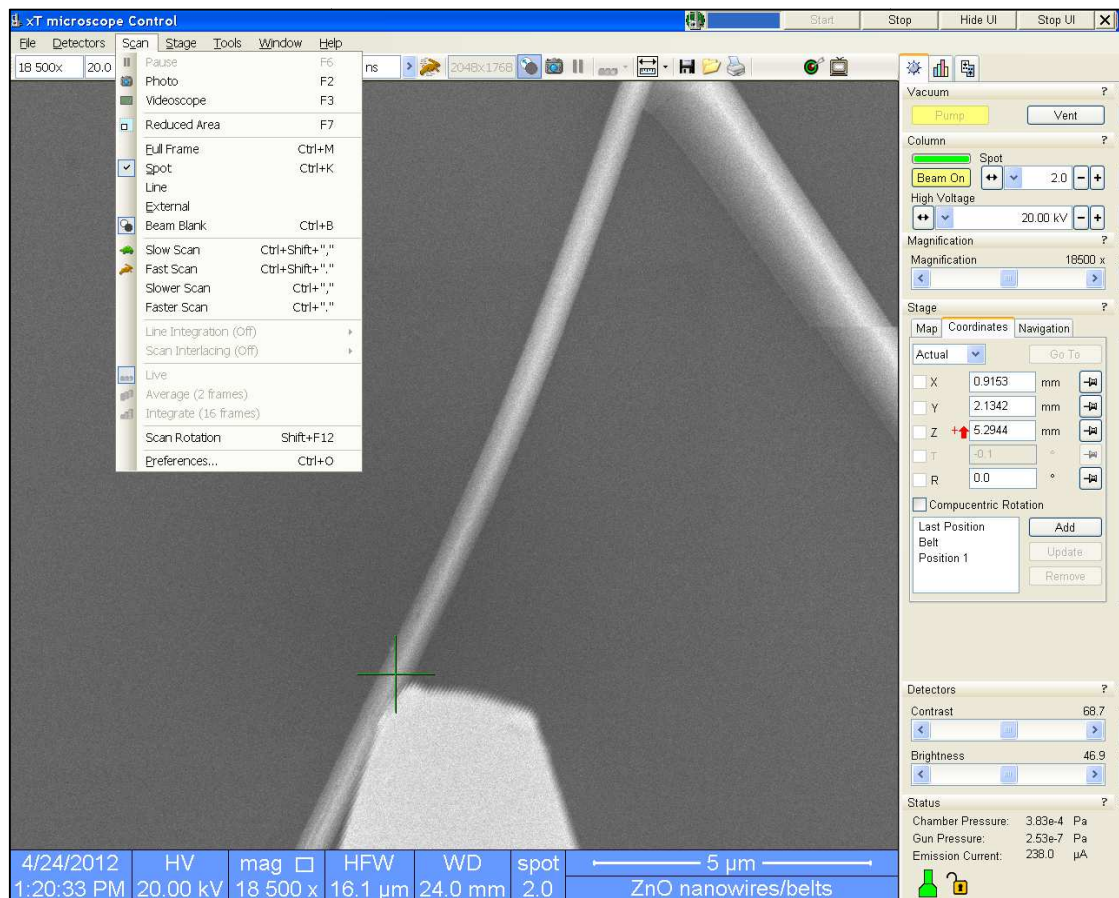


Figure 15. xT Microscope Control screenshot. The full frame, line, and spot mode are option under the Scan drop-down menu. The cross-hairs appear and the frame stops updating. The image is at 18500x magnification. The spot size is 2.0, voltage 20.0 kV. Zinc Oxide nanowire and NSOM probe tip are also shown.

12. Sample

The sample consists of Zinc Oxide (ZnO) nanostructures grown by the physical vapor deposition (PVD) process on a Silicon (Si) substrate. The sample was provided by a group led by Prof. Z. L. Wang of the Georgia Institute of Technology. Figure 16 shows the sample mounted prior to being placed in the Multiview 2000 head. Figure 17 shows a high-resolution image of the nanostructures on the sample, as seen via the SEM. Figure 18 shows an SEM image taken of individual nanowires grown by the Thermal Evaporation process at the Georgia Institute of Technology.

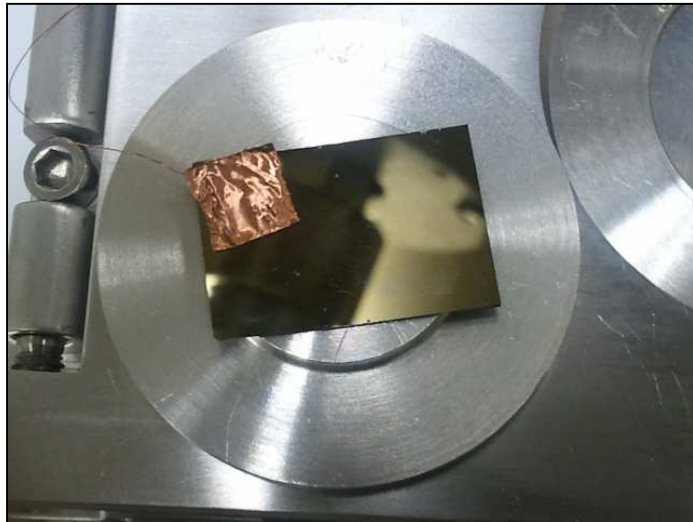


Figure 16. Zinc oxide (ZnO) nanostructures grown by physical vapor deposition (PVD) on silicon substrate. Sample mounted on sample holder by light adhesive. Copper tape and wire electrically grounds sample to NSOM stage.

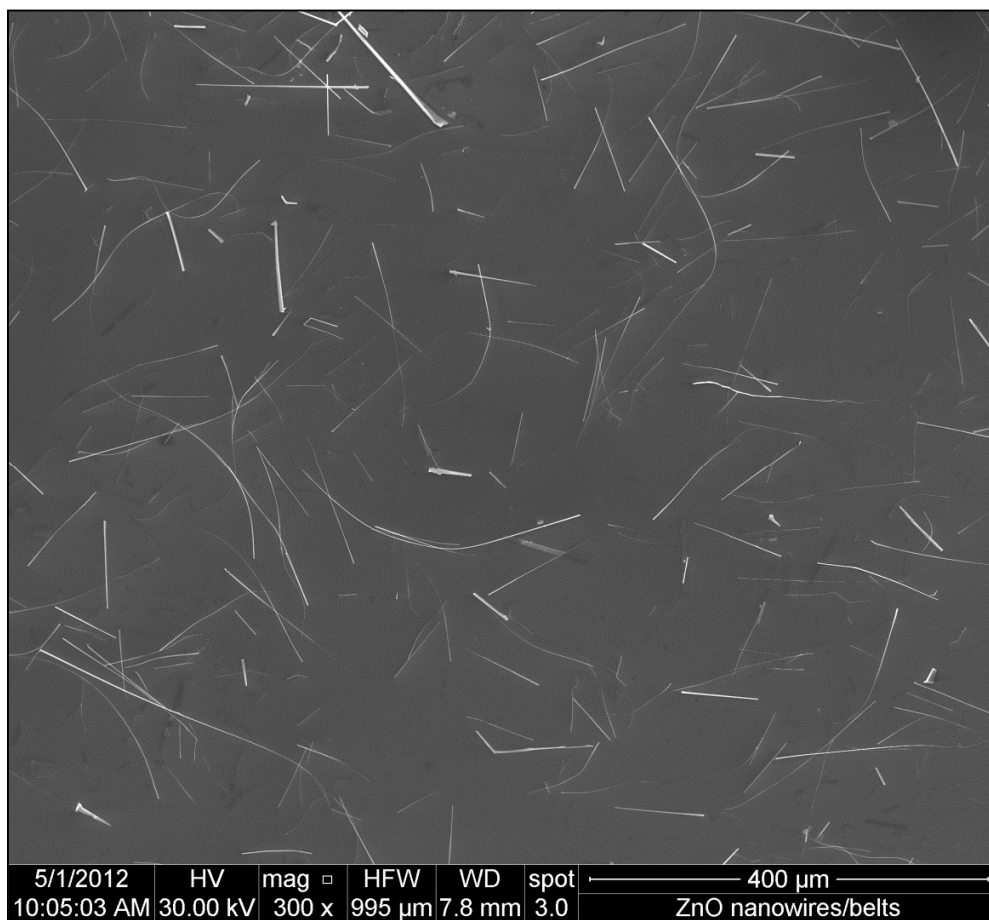


Figure 17. Zinc Oxide (ZnO) nanostructures on a silicon substrate, grown by the thermal evaporation process. Magnification is 300x, working distance is 7.8 mm, spot size of 3.0.

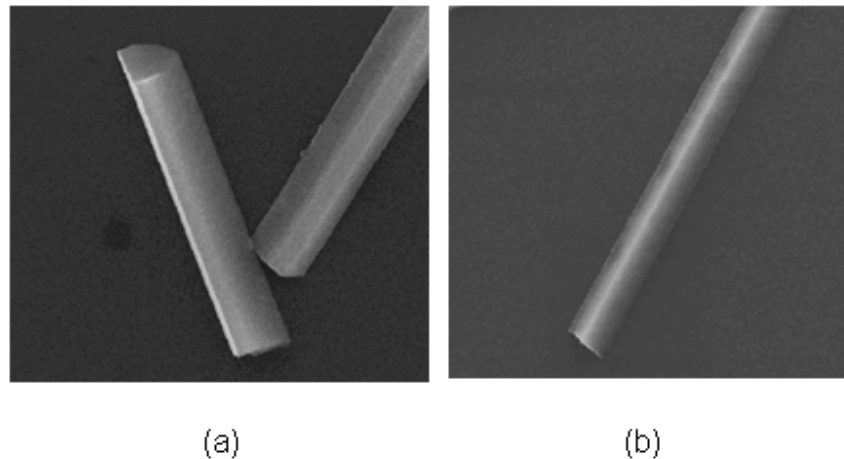


Figure 18. (a) ZnO nanowire, approximately $1\mu\text{m}$ in diameter. SEM Image taken at accelerating voltage of 30kV, magnification 50,000x, spot size 3.0, working distance of 23.9 mm. Image shows 3-D structure of ZnO nanowires. (b) Top down view of ZnO nanowire, approximately $1\mu\text{m}$ in diameter. SEM Image taken at accelerating voltage of 30 kV, magnification 25,600x, spot size 3.0, working distance of 7.9 mm. Image shows ridge along length of wire, common in the structures examined.

B. EXPERIMENTAL METHOD

1. Overview

The principal experimental method involves conducting raster scans of nanostructures using the NSOM/AFM probe tip, while directing a beam of electrons onto the sample from the SEM. Getting the probe tip in proper feedback mode is a central piece of AFM/NSOM work. Once the nanowire of interest is selected, and inertial motion is used to move the probe relatively close to the structure, preparation can be made to lower the probe tip down the z-axis to the sample surface. Inertial motion movement is performed with the probe tip retracted from the surface to reduce the chance of damage during movement of the sample.

2. Lock-In Procedure

A lock-in procedure must be performed to set the resonance frequency of the probe tip prior to any approach to the sample surface. Using the NWS software, the Lock-in Controller selects the resonance curve which determines the frequency, amplitude and a phase of the tuning fork. The Lock-in procedure is initiated from the SPM control tab, as shown in Figure 19.

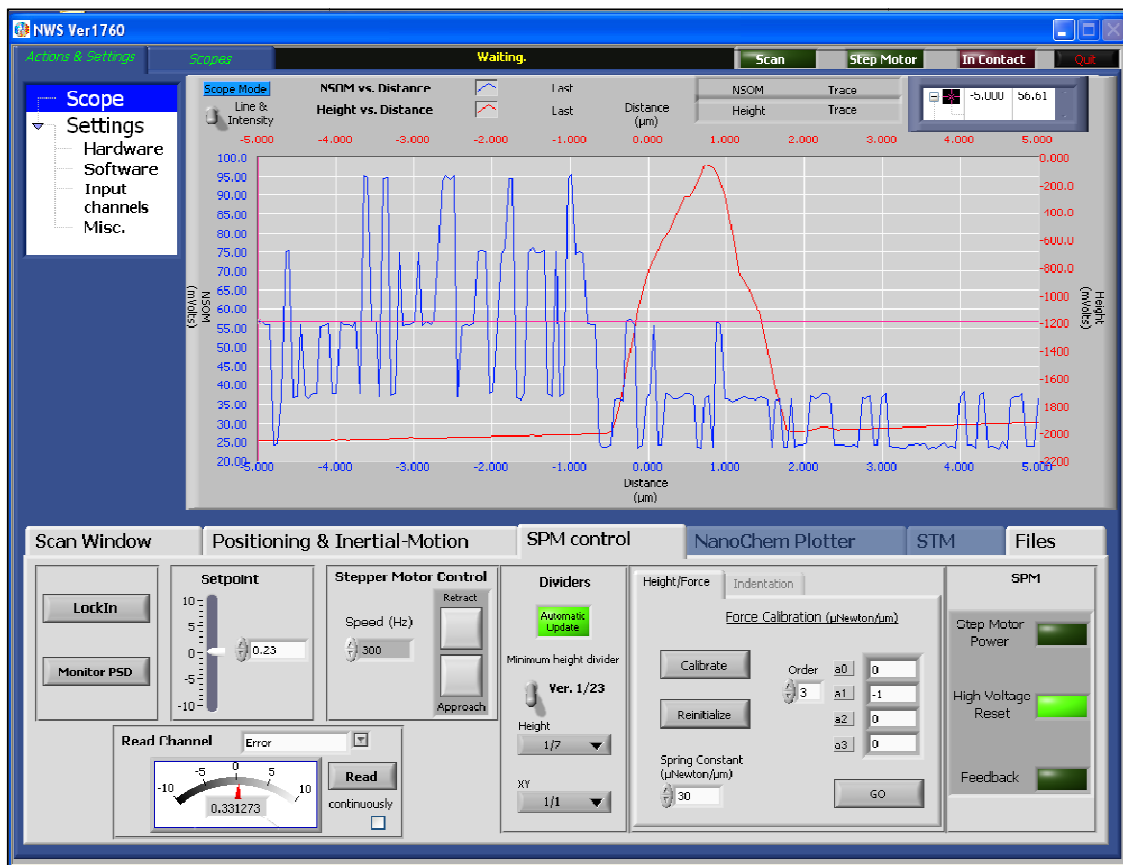


Figure 19. Screenshot from NWS Ver1760 software. Under the SPM control tab, the LockIn, Stepper Motor Control, Setpoint, and Read Channel functions are located. Indications for Scan, Step Motor, and In Contact are located in the upper right.

The Lock-in Procedure is as follows:

1. From the SPM Control tab, select LockIn.
2. Select the Total gain and Oscillation Out 1, based on defaults or the specific characteristics of the sample and probe.
3. Select Phase Feedback as the Feedback Mode.
4. Select Magnitude for the Sweep Signal.
5. Select the frequency range based on the resonance frequency printed on the probe container.
6. Verify that Averaging is set to 1.
7. Click Start to generate the resonance frequency graph.
8. The maximum of the graph should be approximately 8V. The total gain and/or Oscillation Out 1 may have to be adjusted, and the graph. Once the resonance frequency curve is successfully generated, click Set Frequency.
9. Click Autophase.
10. Once the phase sequence is completed, select Squared on the Sweep Signal drop down menu.
11. Click Start to generate a phase versus frequency curve.
12. Move the red cursor on the x-axis to where the curve crosses the zero phase frequency and click Set Frequency.
13. Click Finish.

If done correctly, the resonance frequency graph should look similar to the screen shown in Figure 20.

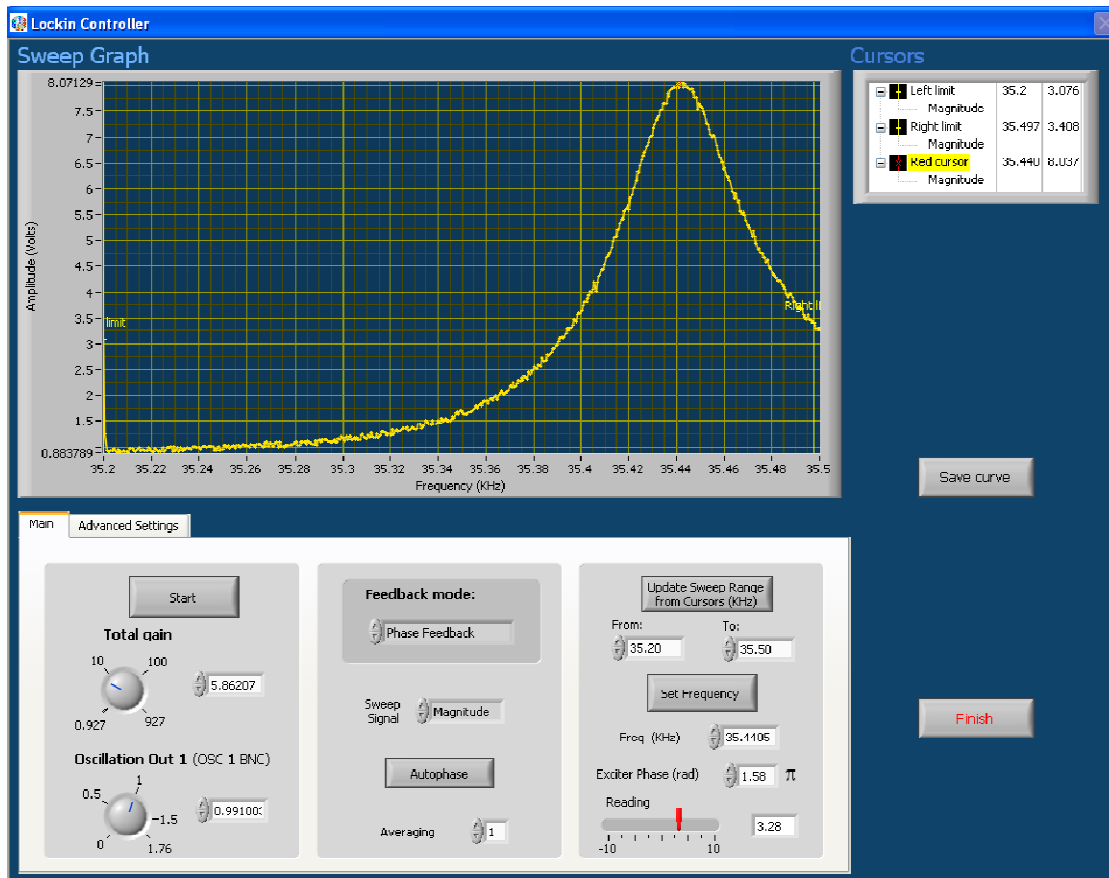


Figure 20. Sweep graph of amplitude versus frequency. The sweep signal is set to magnitude and the feedback mode is Phase feedback. The Total gain and Oscillation Out 1 settings have been adjusted to achieve a maximum amplitude of 8V. In this case, the frequency is set at 35.44 kHz. The Autophase and Set Frequency buttons can also be seen on this screen.

The phase versus frequency graph should look similar to the screen shown in Figure 21.

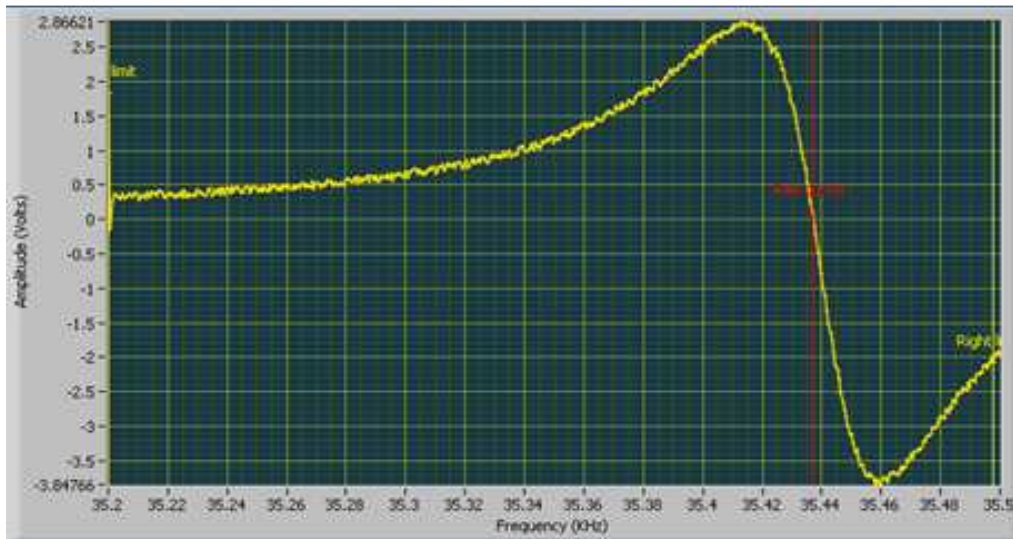


Figure 21. Sweep graph of amplitude versus frequency. The sweep signal is set to Squared and the feedback mode is Phase Feedback. The cursor is moved to where the resonance curve crosses the x-axis. The frequency, in this case, is set at 35.44 kHz.

3. Approaching the Sample Surface

Once the Lock-in procedure is complete, the setpoint must be adjusted before the tip approaches the surface. The setpoint indicates the strength of the force applied to the surface by the probe tip. From the SPM Control tab, the setpoint should be adjusted such that the Error (as read from the Read Channel) is between 0.3 to 0.4V [25]. The probe tip can now be brought in contact with the sample. On the SPM Control tab, under Stepper Motor Control, click Approach. The “Stepper Motor” indicator should illuminate during the approach. The SEM image will also blur as an indication of the movement of the probe tip during the approach.

When the error signal reaches zero, the probe tip is now in contact with the surface. The SEM image will return to normal as the Stepper motor disengages. The “In Contact” indicator illuminates and the “Stepper Motor” indicator are extinguished.

4. Initiating a Scan

Once the probe tip is in contact, a scan window can be determined. Various options are available under the Scan Window tab. The orientation of the scan, size of the scan window, as well as the number of points in the window, and the time spent at each point can be selected from this tab. The number of points in the window and the time spent at each point relate to the resolution of the scan. The orientation of the scan can be selected based on the orientation of the structure being measured and to minimize interference with the electron beam during scans. For example, for a vertically oriented wire, the best raster scan would be such that the fast axis was perpendicular to the long axis of the nanowire. The slow axis would then move down the length of the nanowire. The two raster scans used in this thesis are shown in Figure 22.

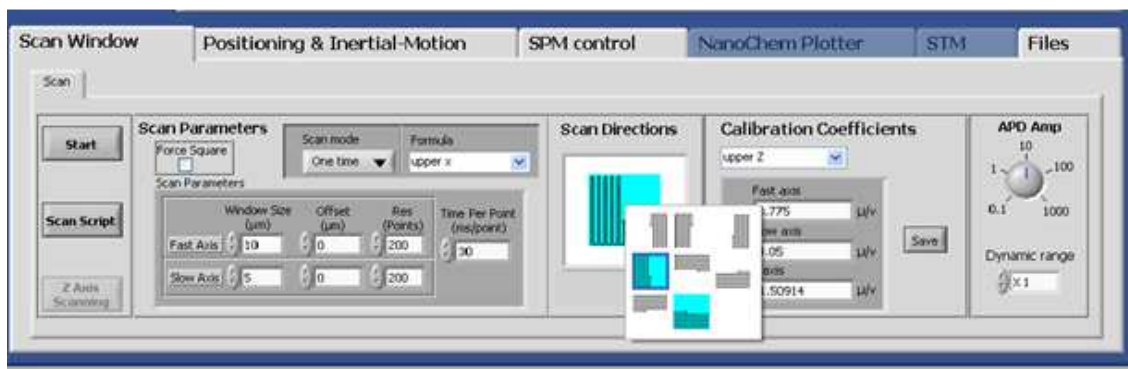


Figure 22. Scan Window. The scan directions of the raster scan, horizontal and vertical, are selected from this tab. The user can also select the size of the fast and slow axis, the number of points, and the time per point, for the scan window. The start button initiates the scan with the selections made.

Once all parameters are set, clicking Scan (or Start) starts the scan. The initial probe position will be the center of the scan window. During the scan the setpoint, low pass filter, proportional gain, integrator, and differentiator may need to be adjusted to improve the AFM signal. Figure 23 shows the typical setting on this portion of the SPM Controller used by the author.



Figure 23. Typical Feedback Gain settings on the SPM Controller. The Low Pass filter and Integrator settings are rotated fully clockwise to the maximum value. The Differential setting is rotated fully counter-clockwise to the minimum value. The Proportional setting is rotated clock-wise to the “10 o’clock” position.

Once the scan is started, the SEM can be placed in spot mode, at the appropriate settings for the experiment, and the carriers produced to create cathodoluminescence in a nanostructure. Data are analyzed with scanning probe microscopy software, WSxM, provided by Nanonics Inc. Using this experimental setup and the methods described in this chapter, control, diffusion length, and waveguiding experiments were conducted.

THIS PAGE INTENTIONALLY LEFT BLANK

III. CONTROL EXPERIMENT

A. OVERVIEW

Due to the orientation of the electron beam with respect to the nanowire being examined and the NSOM probe tip, it was suspected that incidental interaction may occur between the electron beam and the probe tip, which may interfere with accurate minority carrier diffusion length measurements during the raster scan. During incidental direct or scattered interaction, the electron beam would generate photons by cathodoluminescence from the intrinsic luminescence of the fiber probe tip in addition to, or instead of the nanowires being investigated. Despite using an elongated tip that extends further beyond the probe holder, incidental contact may occur between the beam and the probe tip. There exists, therefore, a potential trade-off in measuring the diffusion length using the technique involved in this thesis. As the probe tip gets closer to the generation site, there is a greater chance of direct and scattered electrons from the finite size beam interacting with the NSOM probe tip. The further the probe tip scan starts from the generation site, the less accurate any measurement of the diffusion length would be, as electrons and holes would recombine and emit light away from the probe tip and may not be collected. Essentially, relevant data are lost by not starting the raster scan as close to the generation site as possible.

The electron beam at the sample surface is not a point source, but is very narrow and is not believed to contribute greatly to the electron beam and probe tip overlap. The theoretical electron beam diameter for the spot sizes used in this thesis is approximately 2 nm at a working distance of 10 mm. The actual diameters for electron beams are proprietary information of FEI Incorporated and varies with applied voltage, spot size (probe current), and working distance. Figure 24 shows the relative position of the electron beam and the probe tip during the raster scan for the case of the beam being far away from the probe. This position minimizes the signal generated by any probe tip / electron beam

interaction. Since the probe tip is far from the generation site, the diffusion length measurements lose considerable accuracy, and are limited in measuring the shortest diffusion lengths.

In contrast, Figure 25 shows the optimal starting positions for the probe tip and electron beam for accurate measurement of diffusion length. With the probe tip and electron beam in close proximity, the largest amount of light data from the generation site can be captured by the NSOM. With this configuration, the chance of the electron beam interacting with the probe tip increases. The signal interference could be significant if measuring a nanowire with relatively low luminescence.

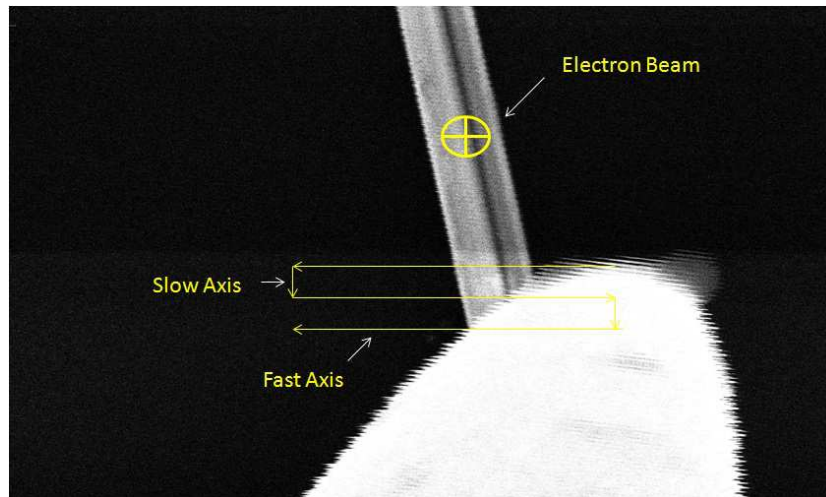


Figure 24. Relative position of electron beam and probe tip on a nanowire at $\sim 20000\times$. The electron beam is placed on the nanowire in spot mode. The probe tip is away from the electron beam and performing a raster scan of the nanowire featured. Some diffusion length data are lost by starting the probe tip far away from the cathodoluminescence generation site.

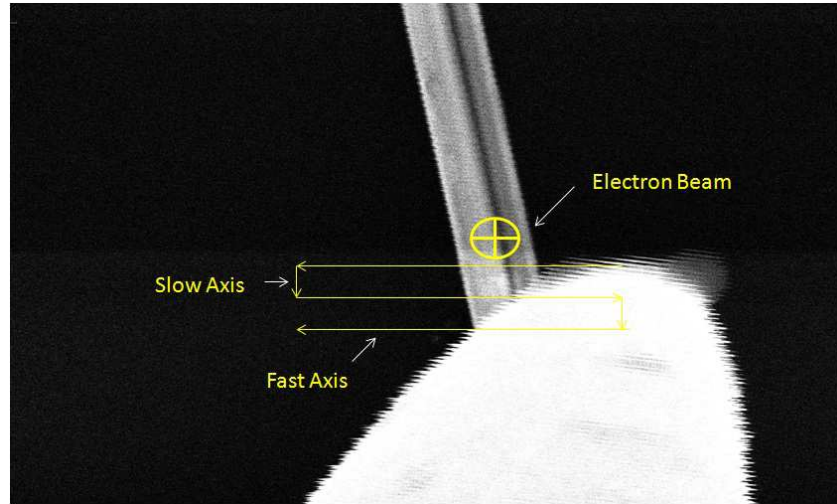


Figure 25. Relative position of electron beam and probe tip on a nanowire at $\sim 20000\times$. The electron beam is placed on the nanowire in spot mode. The probe tip is away from the electron beam and performing a raster scan of the nanowire featured. By placing the probe tip close to the electron beam, the chances of incidental contact increase. The risk increases that photons would be generated in the probe tip vice the nanowire being investigated and bias diffusion length results. This phenomenon would be more pronounced when measuring a low luminescent material.

A method was needed to maximize the intensity data read by the NSOM tip while minimizing the interference caused by the interaction of the electron beam and the probe tip. The method chosen was to measure the cathodoluminescence of the probe tip and selectively filter that optical signal. With appropriately chosen filters, the luminescence from the large bandgap nanowires could reach the photomultiplier while significantly reducing the signal generated by the probe tip.

B. EXPERIMENTS

1. Control Raster Scan

To test the background signal that may be biasing the result, a control experiment was conducted. The control experiment scanned a $2\text{ }\mu\text{m}$ (fast axis) $\times 10\text{ }\mu\text{m}$ (slow axis) window of silicon (Si) substrate that did not contain any

nanowires. A 20 kV, spot size 3, electron beam was placed 1 μm up the probe tip and the NSOM probe performed a downward raster scan. The experiment was performed for 5 trials. Figure 26 shows the NSOM probe that was used in the control experiment. The measurement overlay indicates that the electron beam was placed 1 micron up from the tip of the probe end.

Figure 27 shows the NSOM data profiles along the slow axis for the five control experiment trials. The five trials show reproducibility among the profiles generated for the trials under similar conditions. The intensity starts at some value and then increases as the probe tip scans downward toward the electron beam. The author believes that this is expected and could be explained by an increased efficiency in optical coupling closer to the probe tip. Figure 28 shows the region more clearly.

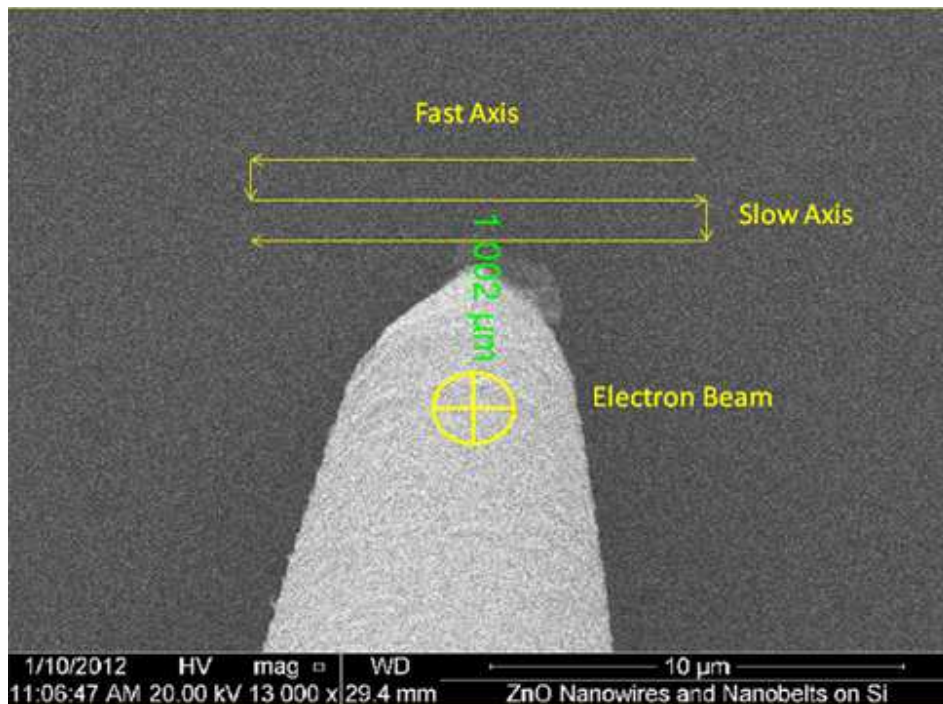


Figure 26. NSOM probe tip with 300 nm aperture at 13000x. The scan window is composed of the Si substrate without any nanowires. The overlay shows the length measurement (green) used to place the electron beam to perform the control experiment raster scan. The fixed electron beam and the path of the probe's downward raster scan are shown (yellow) for illustration.

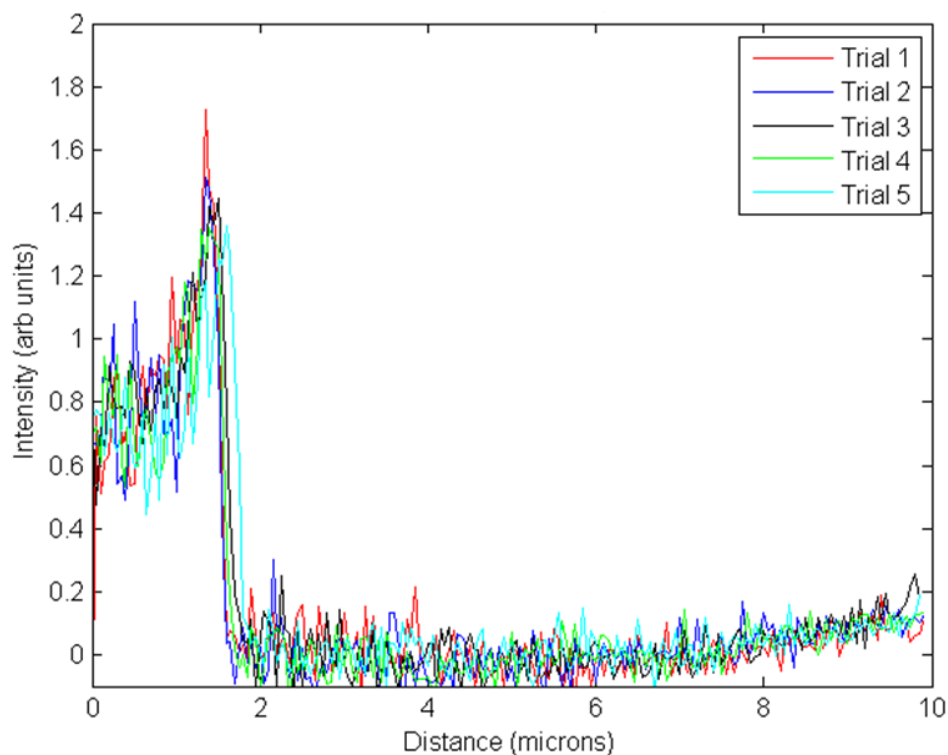


Figure 27. NSOM profile data for five control experiment trials. Intensity, in arbitrary units, is plotted on the vertical axis. Distance, in microns, is plotted on the horizontal axis. The intensity increases as the raster scan progresses and the electron beam is closer to the tip of the probe. Once the probe tip scan path progresses beyond the fixed electron beam position the intensity drops precipitously. Outside of approximately $1\mu\text{m}$ from the electron beam, the NSOM signal has decayed to zero.

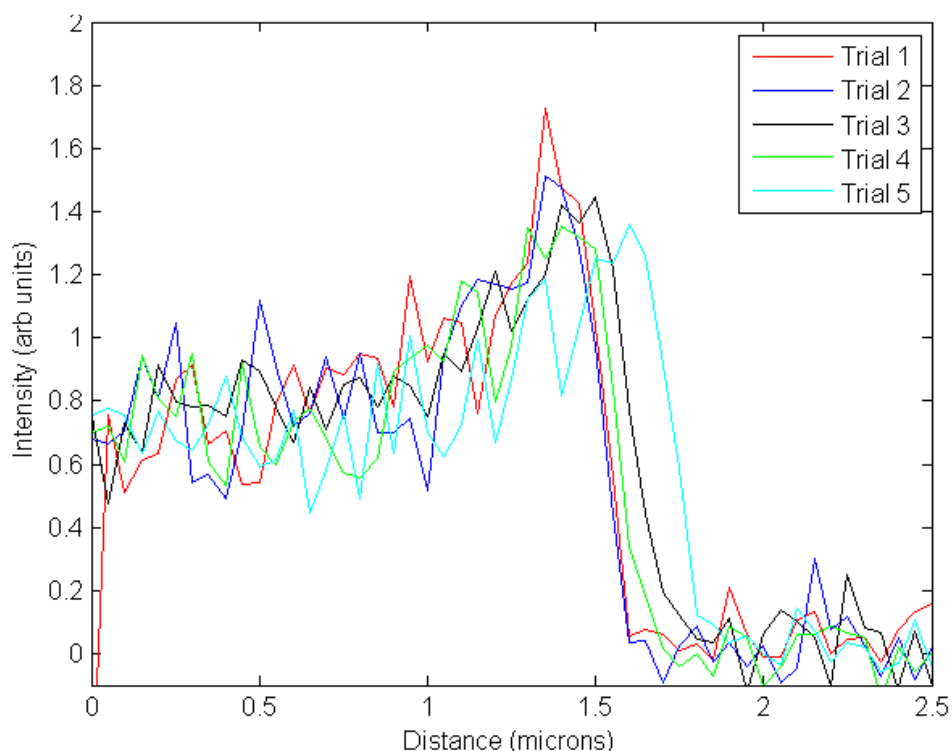


Figure 28. Data from Figure 27, focusing on the region between zero and 2.5 μm .

Once the probe tip has scanned passed 1 μm , the electron beam is no longer directly incident on the probe tip. However, Figure 27 shows that the intensity signal from the NSOM signal continues to increase for another $\sim 0.3 \mu\text{m}$. The author believes this behavior could possibly be explained by the increased optical coupling efficiency as well as scattering and spreading of the generation volume of electrons. What becomes clear, past 1.5 μm in the scan, is that the NSOM intensity drops rapidly toward the background level (zero). As the control experiment shows, in the absence of semiconductor nanowires, the combination of the raster scan and the beam interaction with the probe tip, results in a decaying signal near the incident beam. This decaying signal could bias the results of the diffusion length measurement in a low luminescent material, if the signal from the probe tip was significant compared to the signal from the nanowires. Light generated directly in the probe tip had to be evaluated and ultimately discriminated in order to ascertain that the light intensity versus

distance behavior observed when measuring nanowires was due solely to the diffusion of and luminescence from carriers in nanowires and not based on an artifact of the measurement method itself.

2. Cathodoluminescence of Probe Tip

A portion of the silicon based fiber optic probe was stripped of its plastic coating and placed in the JEOL 840A Scanning Electron Microscope (SEM). Cathodoluminescence (CL) was performed with an electron beam voltage of 30 kV and probe current of 1×10^{-9} A. The light was collected with a parabolic mirror and dispersed with a $\frac{1}{4}$ -meter monochromator to determine the spectrum of the luminescence from the probe tip. The cathodoluminescence of the probe tip as function of wavelength is shown in Figure 29. The largest peak is located between 400 nm and 500 nm.

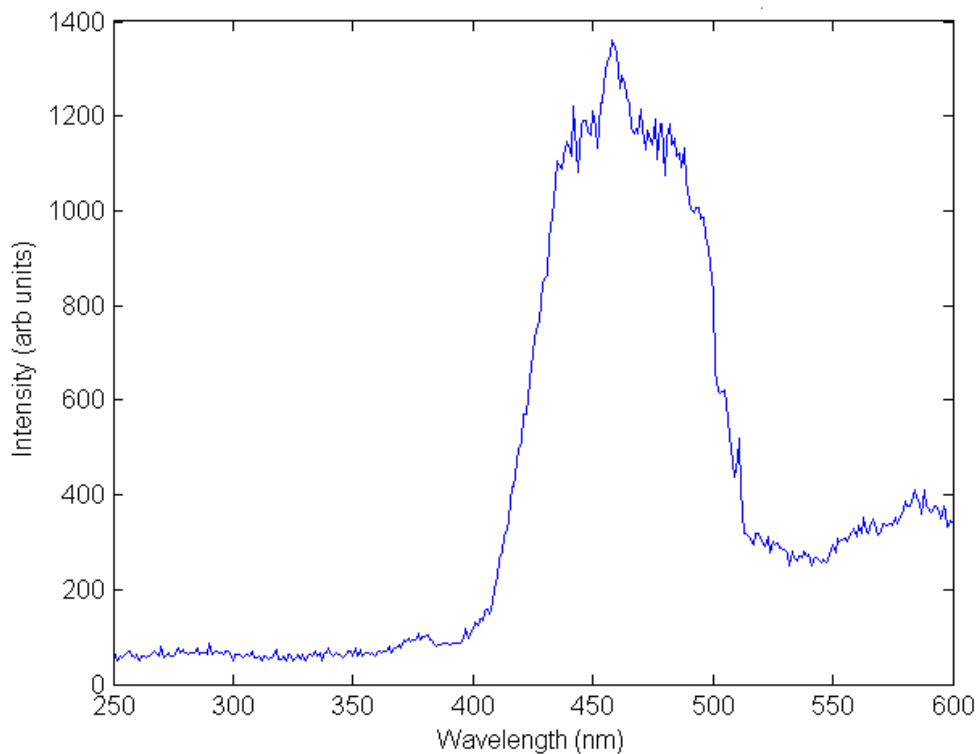


Figure 29. Cathodoluminescence for the silicon based NSOM/AFM probe tip. Intensity, in arbitrary units, is plotted on the vertical axis. Wavelength, in nanometers, is plotted on the horizontal axis.

C. FILTERS SELECTION

Based on the luminescence results, two filters offered by the Andover Corporation were selected. The 400FL07 is a 400 nm short-pass filter that transmits photons with wavelengths shorter than 400 nm while attenuating longer wavelength light. Beyond approximately 430 nm, the transmission percentage is effectively zero. The performance curve of the 400 nm short-pass filter was provided by the manufacturer and is shown in Figure 30.

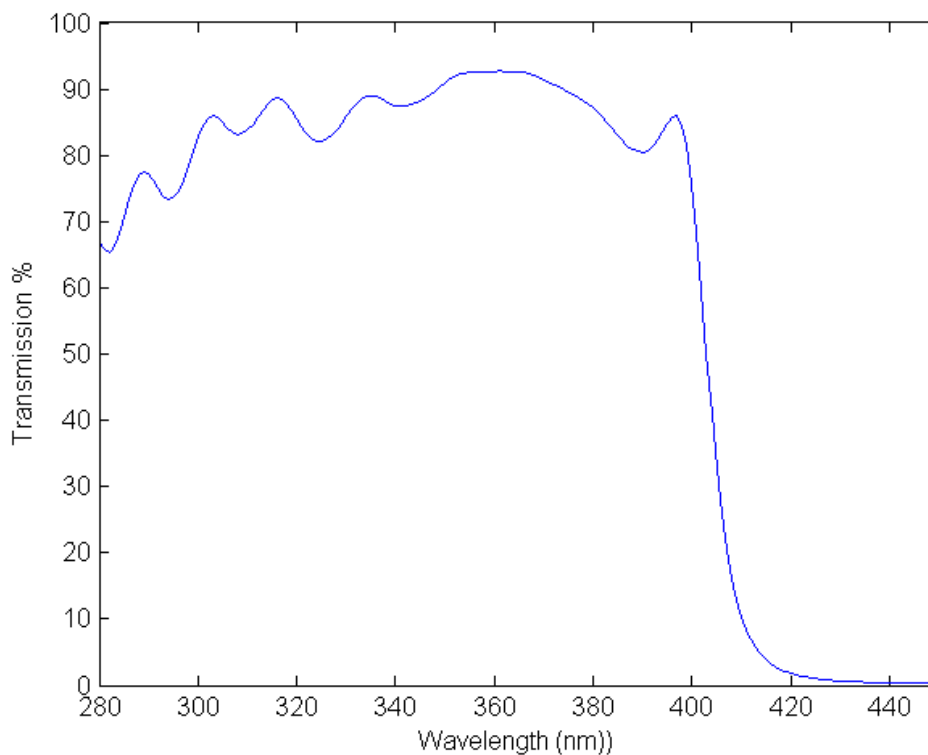


Figure 30. Filter performance for 400FL07 short-pass filter offered by Andover Corporation. Transmission percentage is on the vertical axis. Wavelength, in nanometers, is on the horizontal axis. The 50% transmission point is 400 nm.

The 400 nm short-pass filter alone does not remove the entire CL spectrum of the probe tip featured in Figure 29. Beyond approximately 450 nm, the transmission percentage begins to rise again. A second filter was required.

The 450FL07 is a 450 nm short-pass filter that will attenuate light with wavelengths greater than 450 nm. Figure 31 shows the transmission performance curve for this filter, as provided by the manufacturer.

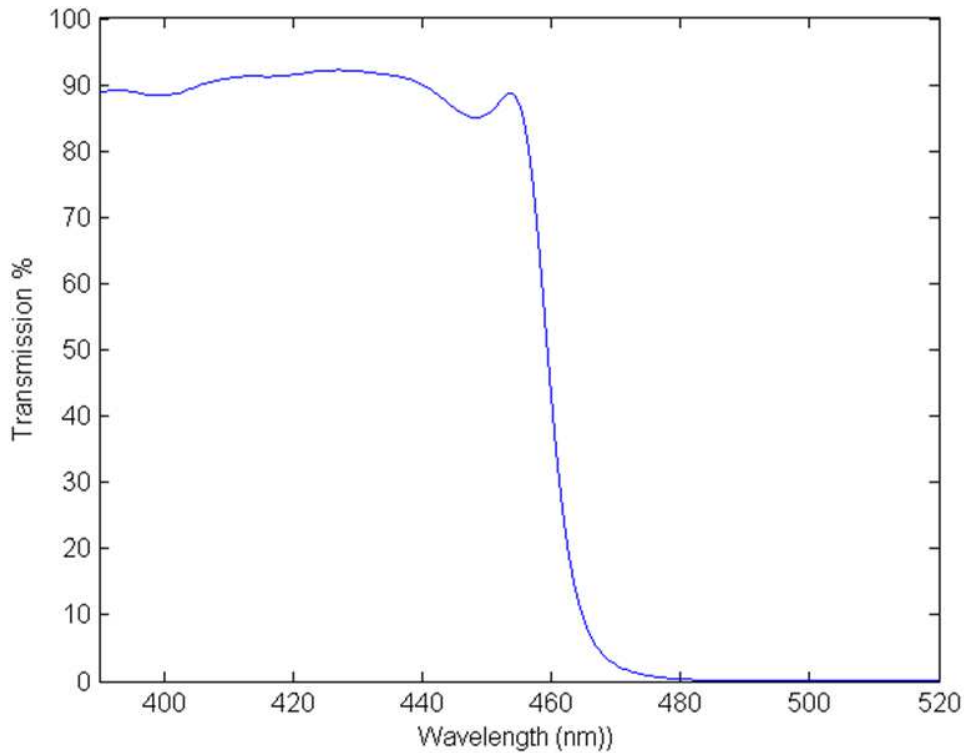


Figure 31. Filter performance for 450FL07 short-pass filter offered by Andover Corporation. Transmission percentage is on the vertical axis. Wavelength, in nanometers, is on the horizontal axis. The 50% transmission point is 450 nm.

1. Theoretical Filter Performance

The two filters were used in conjunction with each other. The single 400 nm short-pass filter was insufficient as the transmission percentage tends to increase at longer wavelengths beyond the data range provided (i.e., beyond 450 nm). The second filter was required to extend the effective range of the filtration. The light from the NSOM would first pass through the 450 nm short-pass filter and then the 400 nm short-pass filter in route to the photo-multiplier tube and counter. The two filters would combine to extend the filtered range but

would also lower the transmission percentage in the overlapped range. The resulting filter performance is a combination of Figure 30 and Figure 31 and is shown as the blue line in Figure 32. The filter transmission percentage was developed by multiplying the overlapping regions together of the individual filters. The majority of the probe tip signal lies in the range of near zero transmission percentage, while the nanowire luminescence of interest for ZnO is approximately 370 nm [29], where the net transmission should be ~70%.

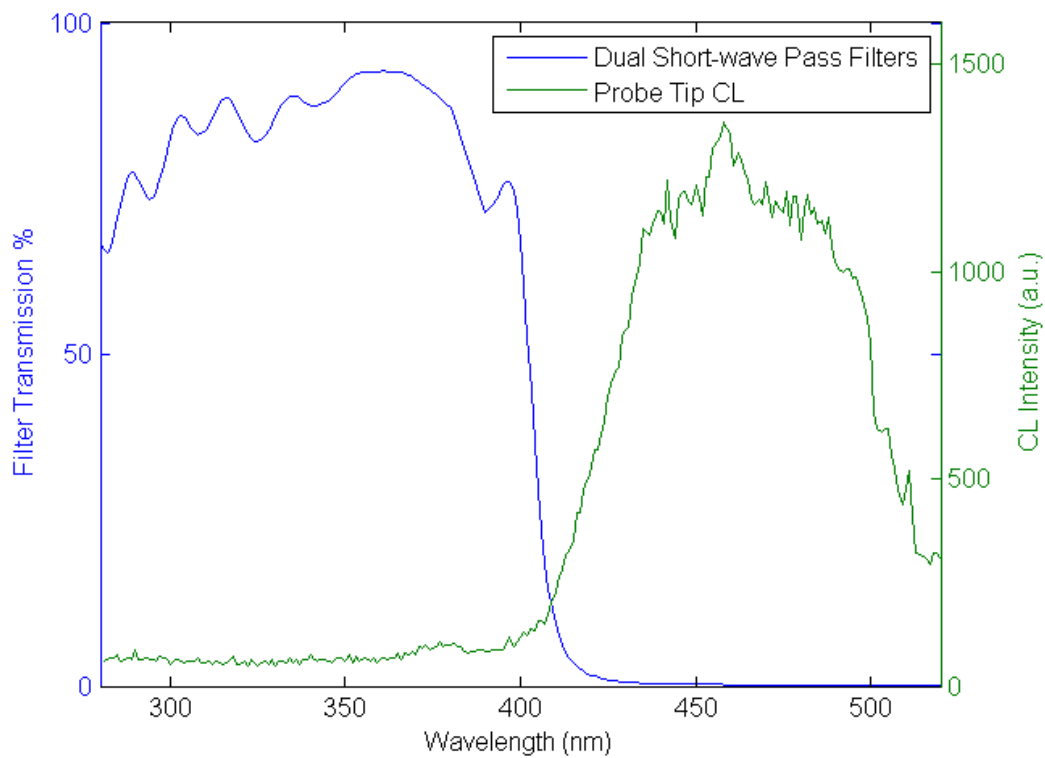


Figure 32. Combined transmission percentage with 400 nm and 450 nm short-wave pass filters (blue) and the cathodoluminescence (CL) spectrum for NSOM/AFM probe tip (green), calculated from data provided for each filter by the manufacturer. The vertical axis is transmission percentage for the filters and the CL intensity of the probe tip. The horizontal axis is the wavelength in nanometers.

2. Measured Filter Effectiveness

The filter performance previously considered was based on data provided by the manufacturer. The actual performance was measured to verify effectiveness of the filter in removing NSOM probe signal. This was done by performing the control experiment without filters, with only the 400 nm filter, and then with both the 400 nm and 450 nm filters installed. The arrangement of the two filters is shown in Figure 33. All other conditions remained fixed in this control experiment. Figure 34 shows that the filters successfully attenuated the cathodoluminescent signal generated by the probe tip. A single filter reduced the signal to approximately one-third its original value. With both filters installed, the CL signal generated by the AFM/NSOM probe tip has been reduced an order of magnitude and is close to the background value (zero).

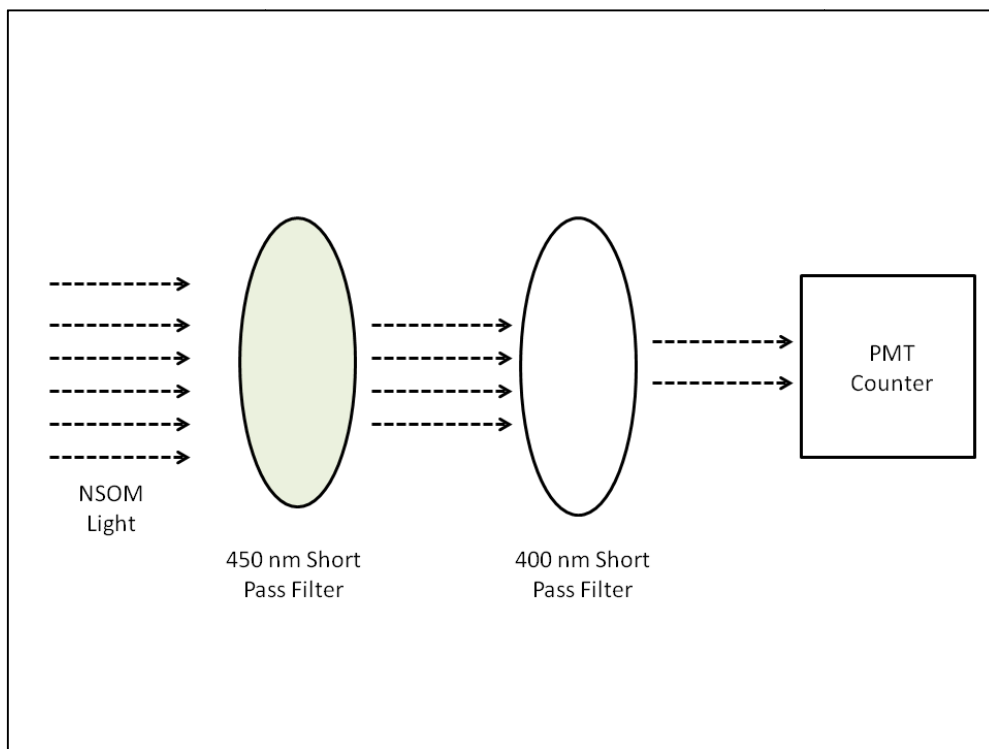


Figure 33. The dual filter arrangement. Light travels from the NSOM via fiber optic wire and is then filtered by the 450 nm short-pass filter and then the 400 nm short-pass filter before entering the photomultiplier tube (PMT).

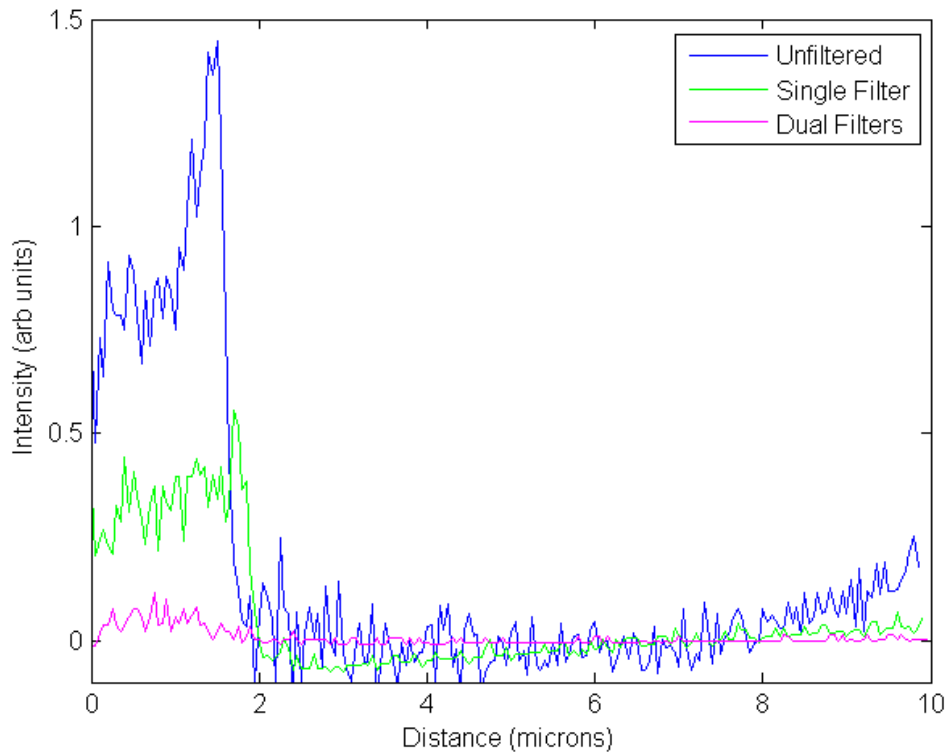


Figure 34. Control experiment conducted to verify performance of filters. Intensity, in arbitrary units, is plotted on the vertical axis. Distance, in microns, is plotted on the horizontal axis. The signal generated in the first two microns of the scan, where the probe tip contribution is believed to be is reduced by the use of the filters. The 400 nm filter alone reduced the signal to one-third the original value. The use of both filters reduced the original signal an order of magnitude.

3. Filter Impact on the ZnO Cathodoluminescence Signal Received

A test was performed to measure the signal loss from the actual semiconductor nanowires due to the use of both filters. A $10\mu\text{m}$ (fast-axis) \times $5\mu\text{m}$ (slow-axis) scan of a 690 nm thick ZnO wire was measured with a 250 nm aperture probe tip. The incident beam had an accelerator voltage of 20 kV and spot size 2. The test was performed once with the filters and without the filters. The slow axis profile is plotted in Figure 35. Figure 35 shows that the signal from the ZnO wire is attenuated by about 25% by the use of the combined filters. The

filters reduce the signal from the NSOM/AFM probe tip by an order of magnitude while only losing ~30% of the signal from the semiconductor. The author believes that a similar response would be achieved for semiconductors with bandgaps, and therefore wavelengths, near ZnO. These filters were used in the remainder of the thesis.

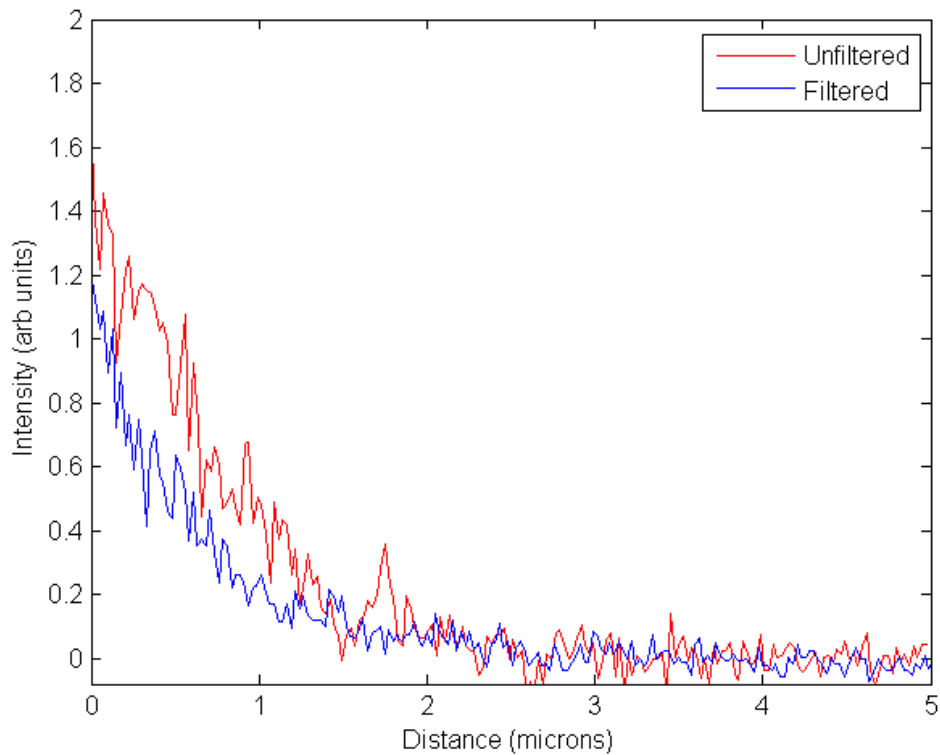


Figure 35. The effect of adding both 400 nm and 450 nm short-pass filters to the path to the PMT for the CL of a ZnO nanowire. Intensity, in arbitrary units, is plotted on the vertical axis. Distance, in nanometers, is plotted on the horizontal axis. The signal is reduced by approximately ~30%.

THIS PAGE INTENTIONALLY LEFT BLANK

IV. DIFFUSION LENGTH MEASUREMENTS

A. DIFFUSION LENGTH AS A FUNCTION OF NANOWIRE DIAMETER

1. Overview

This experiment measured excess carrier diffusion lengths in ZnO nanowires, of varying diameters, and analyzed whether there was any correlation between the wire diameter and diffusion length.

2. Settings

Spot size was reduced to 2 for this experiment to minimize the SEM charging effects that tended to cause the electron beam to drift off the nanowire, biasing results. Accelerating voltage was held constant at 20 kV.

A 250 nm aperture NSOM/AFM probe was used for this experiment. Thinner probe tips achieve more precise AFM data, but significantly less light is received by the NSOM. Time constant and count rate can be adjusted to increase the NSOM signal. In this instance, count rate and time constant remained at 1.0 kHz and 2.0 ms, respectively.

3. Method

a. Diameter Measurements

Diameter measurements were taken using a distance overlay provided by the SEM software. Measurements were taken local to the scan site. Wires were chosen whose width did not vary significantly over the length of the wire.

b. Scanning Cathodoluminescence

The NSOM/AFM probe was brought into contact with the nanowire and a 10 μm (fast-axis) x 5 μm (slow-axis) scan was conducted. The SEM was brought into spot mode and electron beam was directed, via the crosshair graphic user interface. The electron beam was directed on to the nanowire

where the probe crossed the nanowire. The scan was completed and height and intensity versus distance data analyzed with WsXM. In some instances, multiple trials were conducted to get a complete data set.

c. Analyzing Data

In WsXM, the height data provided by the AFM and the intensity data provided by the NSOM are analyzed. Figure 36 shows the data as seen in WsXM. An intensity profile of the NSOM data is created along the axis of the wire. The AFM data is used to verify the axis of the wire. Figure 37 shows a screen shot of the profile created along the axis of a nanowire.

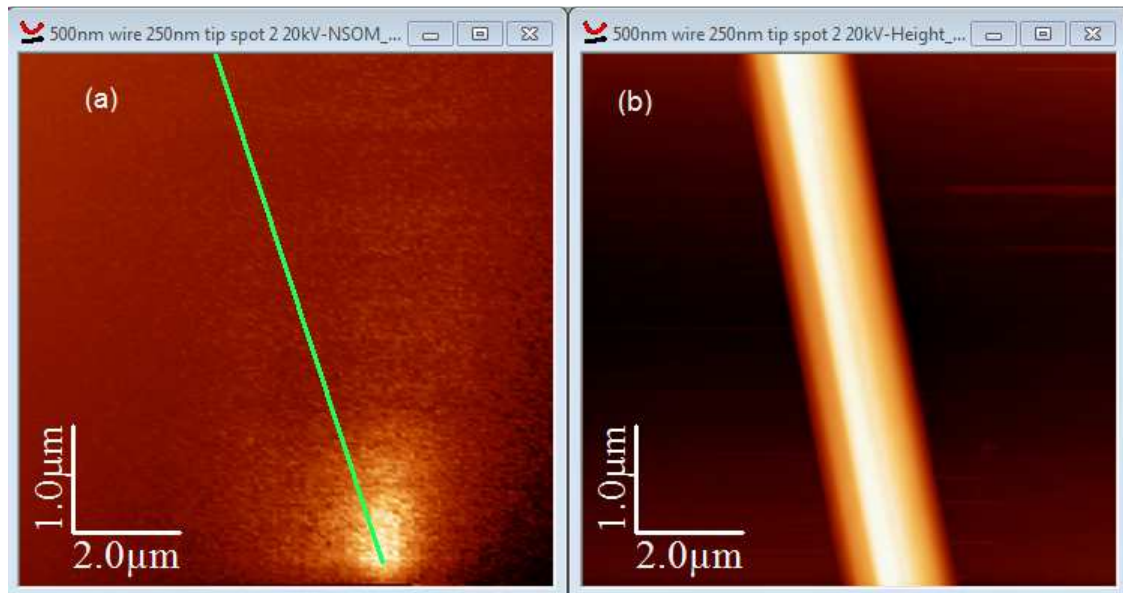


Figure 36. (a) Intensity plot of NSOM data. Brighter and more dense color indicates higher light intensity. A profile (green) is taken along the axis of the wire.(b) Intensity plot of AFM height data. Brighter colors indicate a higher elevation of the nanowire topography.

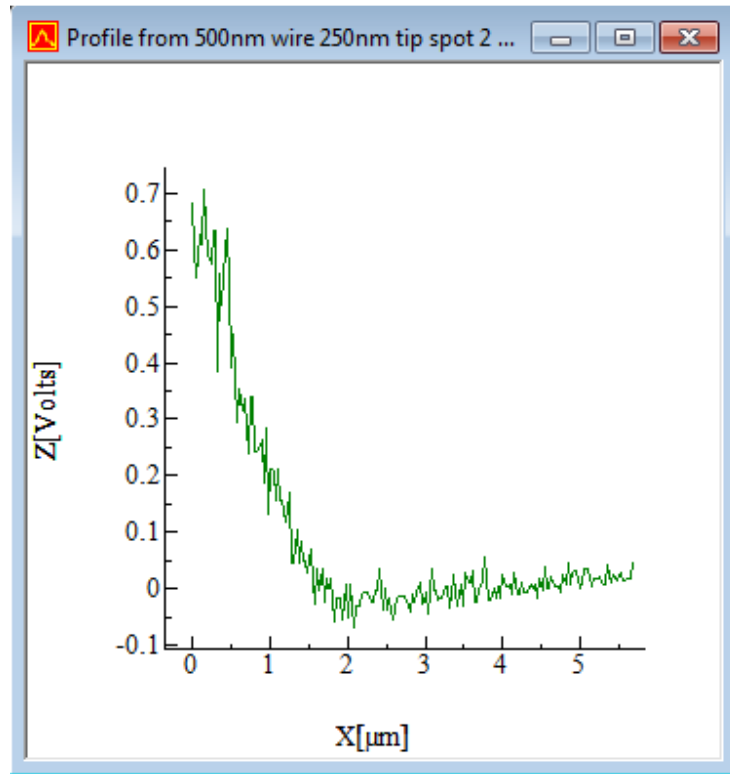


Figure 37. The profile generated from NSOM intensity data. The graph axes are intensity as function of distance.

The profile data from Figure 37 is then converted into a text file to be quantitatively analyzed. The data are normalized and then plotted on a semi-log plot of intensity versus distance. A linear best fit line is generated in which the negative inverse of the slope is taken as the diffusion length. This is readily seen from Equation 5, the one-dimensional diffusion length equation.

WsXM can also produce three-dimensional depictions of the NSOM and AFM data separately or as overlays. Figure 38 shows the previous NSOM data as a three-dimensional representation.

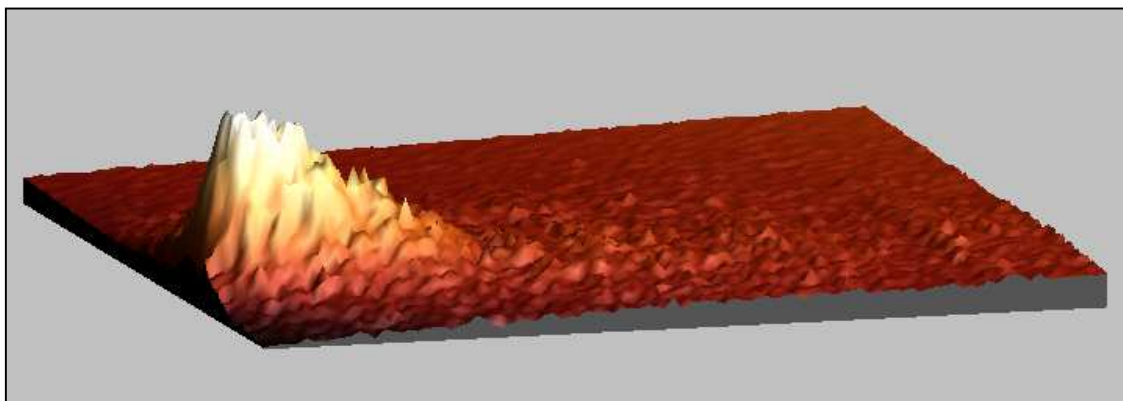


Figure 38. 3D NSOM data showing the decrease of the light intensity as the probe scans away from the generation site along the wire axis

4. Results

Table 1 shows the results for the seven wires measured. The error in the diameter measurement was estimated based on the observed variation in the measurement. The diffusion length error was estimated based on multiple trials and the data from the control experiments. The average diffusion length was calculated to be $0.9 \text{ (+/- } 0.1) \mu\text{m}$. Figure 39 shows the same data graphically as Table 1.

Wire Diameter (nm) (+/- 5%)	$L_D (\mu\text{m})$ (+/- $0.1 \mu\text{m}$)
250	0.6
500	0.5
600	1.0
800	1.2
1000	1.1
1200	1.0
1400	0.9

Table 1. ZnO nanowire diffusion length as a function of wire diameter.

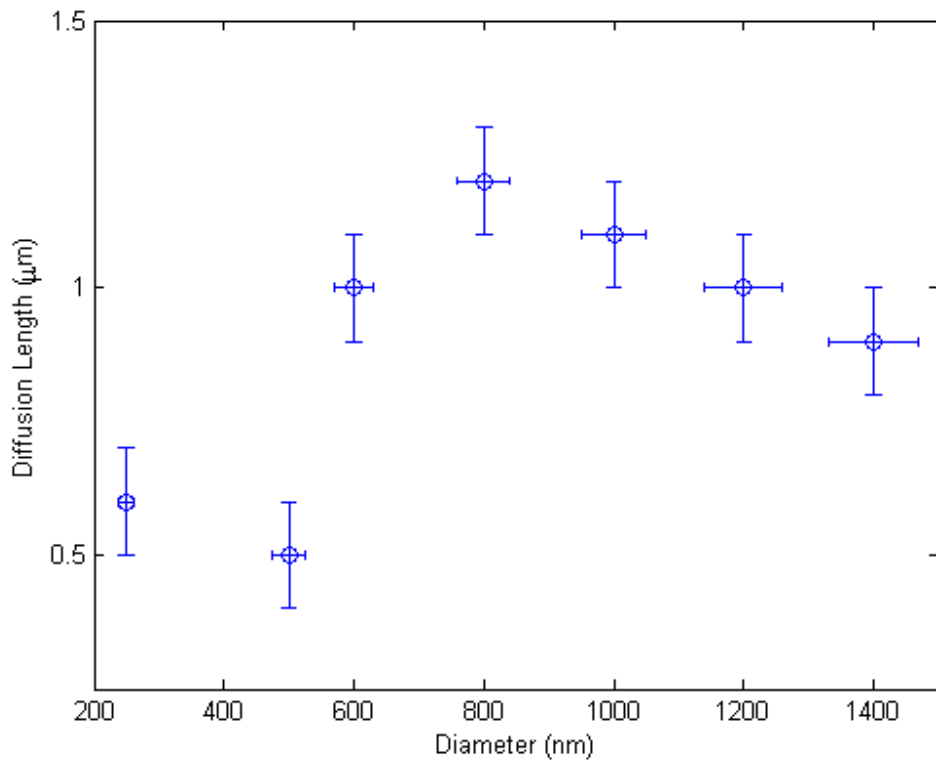


Figure 39. Diffusion length as a function of diameter. Error bars are as indicated in Table 1.

The diffusion length between wire diameters of 200 and 400 nm seems constant at about $0.5\mu\text{m}$. The diffusion length increases with diameter thickness between 500 nm and 800 nm. Between wire diameters of 800 nm and 1400 nm, there is slight lowering, but the diffusion length values are all roughly $1\mu\text{m}$. The general shape is similar to work previously conducted using near field photo current microscopy [30]. Figure 40 shows this previously published work on the diameter dependence of ZnO nanowire diffusion length. The wires used in that study were much smaller than the ones measured in this thesis, but indicate a similar trend. This trend could be explained as arising from the fact that as the diameter of the wire becomes comparable to the diffusion length, the surface to volume ratio may contribute to increased surface effects limiting carrier transport [30].

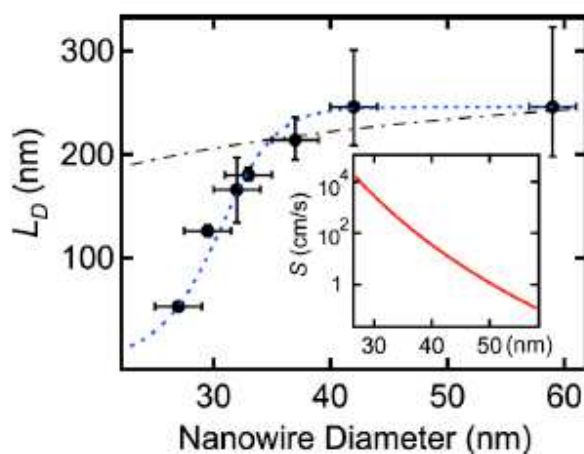


Figure 40. Diffusion length as a function of nanowire diameter. Diffusion length was measured by a near field photocurrent microscopy technique. From [30].

There is a lack of data for ZnO nanowire diffusion length diameter dependency. More data are needed to link the smaller diameter data of Figure 40 to the behavior of the larger diameter wires in Figure 39. The diameter dependence of ZnO nanowire diffusion length could be better modeled with more data in both regions.

V. WAVEGUIDING EXPERIMENTS

A. WAVEGUIDING AS FUNCTION OF SPOT SIZE (PROBE CURRENT)

1. Overview

The waveguiding phenomenon in ZnO has been observed in previous work [31], [32]. Due to a high index of refraction ($n > 2$) and relatively smooth surfaces, one-dimensional semiconductor nanostructures provide high enough reflectivity for photon confinement. This makes the structures of interest as potential lasers and waveguides. Lasing has been initiated with laser excitation, but not yet with electron beam excitation [33]. This experiment images waveguiding output in ZnO nanowires and measures the amount of spreading (FWHM) as a function of nanowire diameter.

Waveguiding can be seen in situ during the an AFM/NSOM scan. Figure 41 shows one example of the ZnO waveguiding as seen from the NWS1760 software interface. The waveguiding output is evident at the end of the nanowire. The light intensity, as indicated in the NSOM data, increases. The end of the wire is indicated by the nanowire topography provided in the AFM height data. The NSOM data suggests that there is light collected on the nanowire surface as the free electrons diffuse and recombine. There is a dark region on the nanowire surface beyond the diffusion region. There is no more light collected from the nanowire surface. At the end of the wire, the light intensity increases considerably. Photons are generated by cathodoluminescence in the ZnO and propagate internally to the ends of the nanowire.

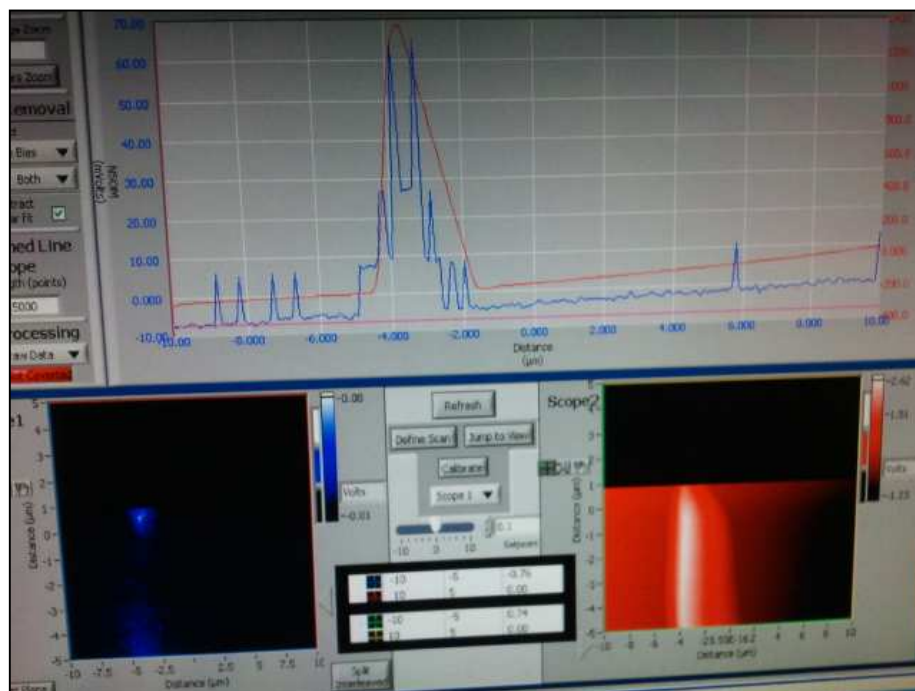


Figure 41. AFM and NSOM data on the NWS1760 software. The top portion of the readout is real time data. The AFM and NSOM are independent but graph on top of each, indicating a common spatial component. This is expected as the light is generated within the wire. The lower two are a waterfall display of the AFM and NSOM data with the newest data at the top. In both views, the AFM data is in red and the NSOM data is in blue. Waveguiding is shown as the NSOM light intensity data increases at the end of nanowire, after the initial surface diffusion. Some light from cathodoluminescence is transmitted internally through the ZnO nanowire.

Having shown that the ZnO nanowires under examination exhibit waveguiding phenomenon, this experiment measured the width of the output distribution as a function of spot size (probe current). Increasing probe current increases the local rate of carrier generation and the intensity of the light.

2. Settings

A 350 nm aperture NSOM/AFM probe was used in this experiment. The time constant was set at 2.0 ms. The count rate was set at 10 kHz. The

combination of the larger aperture probe and increased count rate increased the NSOM signal received. The accelerating voltage remained at 20 kV.

3. Method

a. Waveguiding Scan

A preliminary AFM/NSOM scan was conducted to verify waveguided emission could be observed from a given nanowire. Once a suitable wire was found, usually with a large diameter, the electron beam was placed in spot mode and directed 4 μm above the end of the nanowire. A 6 μm (fast-axis) x 2 μm (slow-axis) scan was conducted on a 730 diameter nm wire, with various spot sizes, ranging from 4 to 7. A smaller scan window was selected to increase resolution. Two trials were conducted.

b. Analyzing Data

The data were analyzed using WxSM. A fast-axis profile was generated, across the portion of the signal with the highest intensity. The data were normalized and a full width at half maximum (FWHM) was calculated for comparison.

4. Results

a. Full Width Half Maximum (FWHM)

Table 2 shows the results for the various spot sizes analyzed. The current and beam diameter were interpolated based on proprietary data provided by FEI Inc. Figure 42 shows a visual representation of the data shown in Table 2. No reduction in FWHM, which would be expected during a transition to lasing behavior, was observed.

Spot Size	Beam Diameter (nm)	Wire Diameter (nm)	Current (pA)	NSOM FWHM (μm)
4	2.4	730	569	0.63
5	3.2	730	2240	1.11
6	5.2	730	8960	0.63
7	9.8	730	35840	0.72

Table 2. The Full Width Half Maximum (FWHM) as a function of spot size.

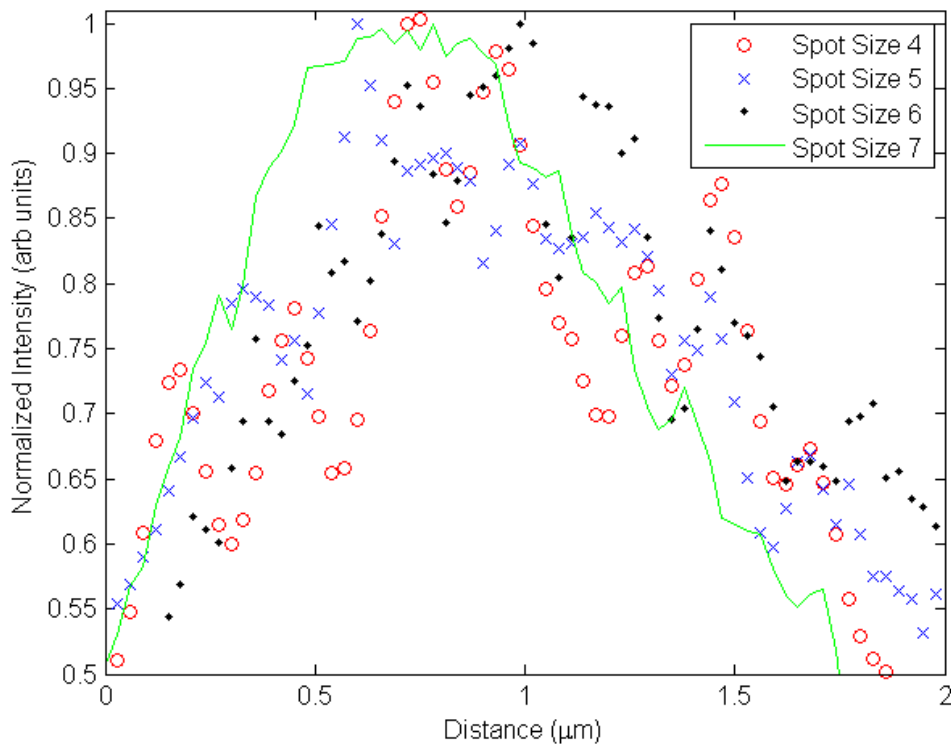


Figure 42. Normalized intensity (arbitrary units) as a function of distance in microns. The intensity was taken from a fast axis profile across the brightest portion of the waveguided signal. This figure shows graphically that the amount of spreading appears to be invariant with the spot size (probe current).

Figure 43 shows three-dimensional views of the NSOM intensity data. It can be seen visually that although the intensity increases as the spot size increases (from left to right), the FWHM of the distribution is uncorrelated.

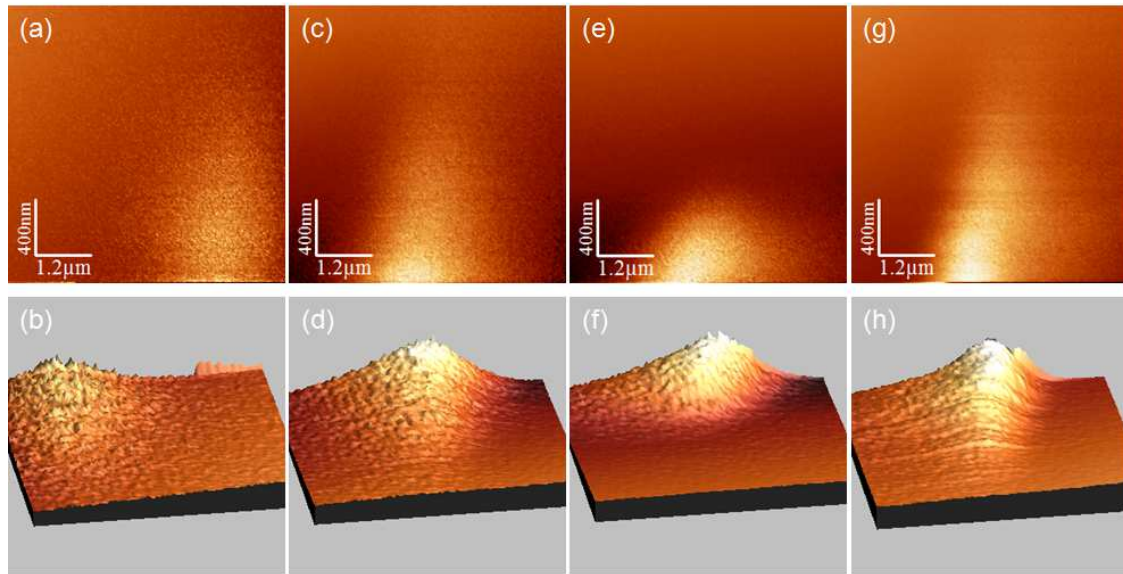


Figure 43. The NSOM data with the 3D version beneath each respective 2D version. Image (a) and (b) are for spot size 4, (c) and (d) for spot size 5, (e) and (f) for spot size 6, (g) and (h) are for spot size 7.

b. Intensity as a Function of Spot Size

The intensity increases as the spot size increases. This result is not surprising as the number of incident electrons increases, the rate of photon creation increases, and the more photons that can be collected during a NSOM scan. The current increases are not linear between spot sizes and neither are the intensity increases. Figure 44 shows the maximum intensity as a function of spot size. Figure 45 shows the maximum intensity as a function of the current from Table 2 on a semi-log plot. The two graphs have similar shapes under these conditions.

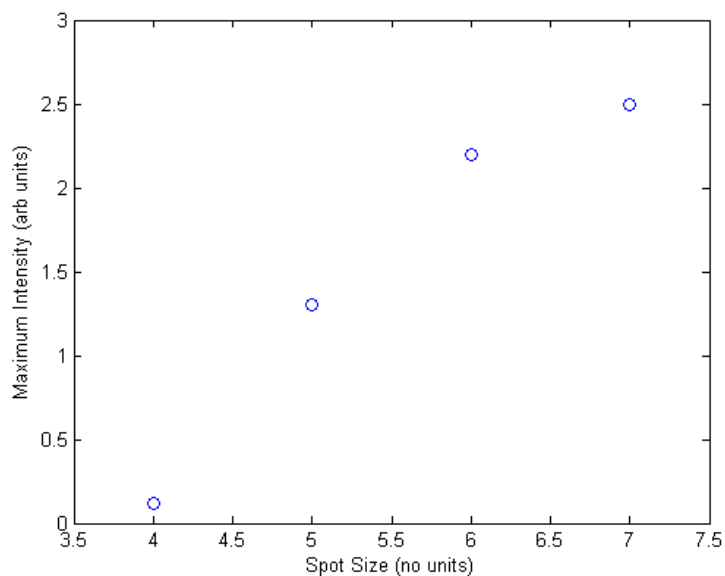


Figure 44. Maximum intensity (arbitrary units) as a function of spot size. Intensity is plotted on vertical axis while spot size is on the horizontal axis. The intensity increases with spot size but is non-linear, particularly at higher spots sizes.

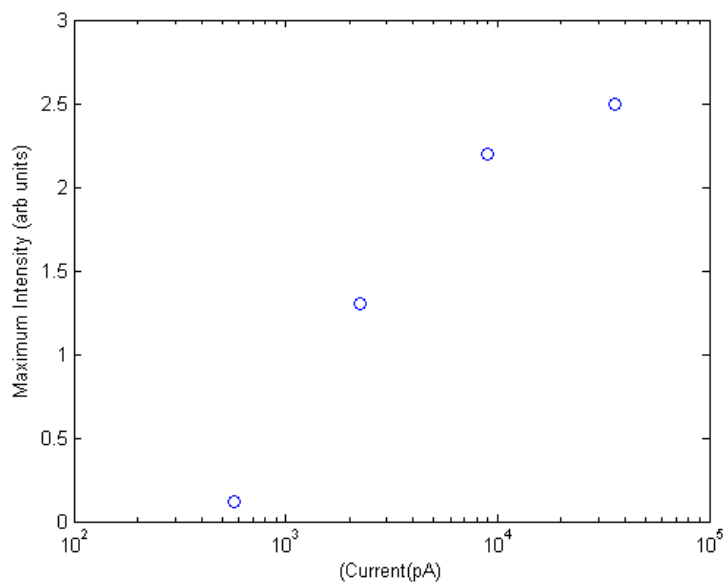


Figure 45. Maximum intensity (arbitrary units) as a function of the current. The intensity is on the vertical axis in arbitrary units. The current, in pA, is on a log-scale horizontal axis. The intensity increases with but is nonlinear, particularly at higher currents.

B. WAVEGUIDING LIMIT AND ESTIMATION OF ABSORPTION COEFFICIENT

1. Overview

The observation of waveguiding and measurement of intensity and FWHM relationship with respect to spot size led to an investigation as to how far the light can propagate within the nanowire and an estimation of the absorption coefficient, α , for near band-edge emission ZnO nanowires.

2. Settings

The accelerating voltage was 20.0 kV. The spot size was set to 4.0. The time constant was set at 2.0 ms. The count rate was set at 10 kHz.

3. Method

a. Measuring Intensity and Distance

A 800 nm wire that exhibited very little curvature was selected. A 6x6 μm scan was conducted at the end of the wire. The electron beam was placed in spot mode on the nanowire, 6 μm from the end of the wire. The distance was measured using the distance overlay provided by the SEM interface. A complete scan was taken and then the beam was moved to a point a greater distance from the end of the wire.

b. Analyzing Data

The NSOM data were analyzed in WsXM. A profile of the NSOM data determined the maximum intensity value at each distance. The data were fitted to an exponential, similar to Equation 6, to estimate the absorption coefficient, α ,

$$I(x) = I_0 \exp(-\alpha x) \quad (6)$$

where I is intensity, and x is the distance to the generation site.

4. Results

a. *Waveguide Limit*

Figure 46 shows a visual representation of the intensity measured by the NSOM as a function of distance, D . It is clear that the intensity decreases with distance and becomes virtually indiscernible from the background signal between 20–30 μm . To first order, this is the waveguiding limit under these conditions for the ZnO nanowire measured.

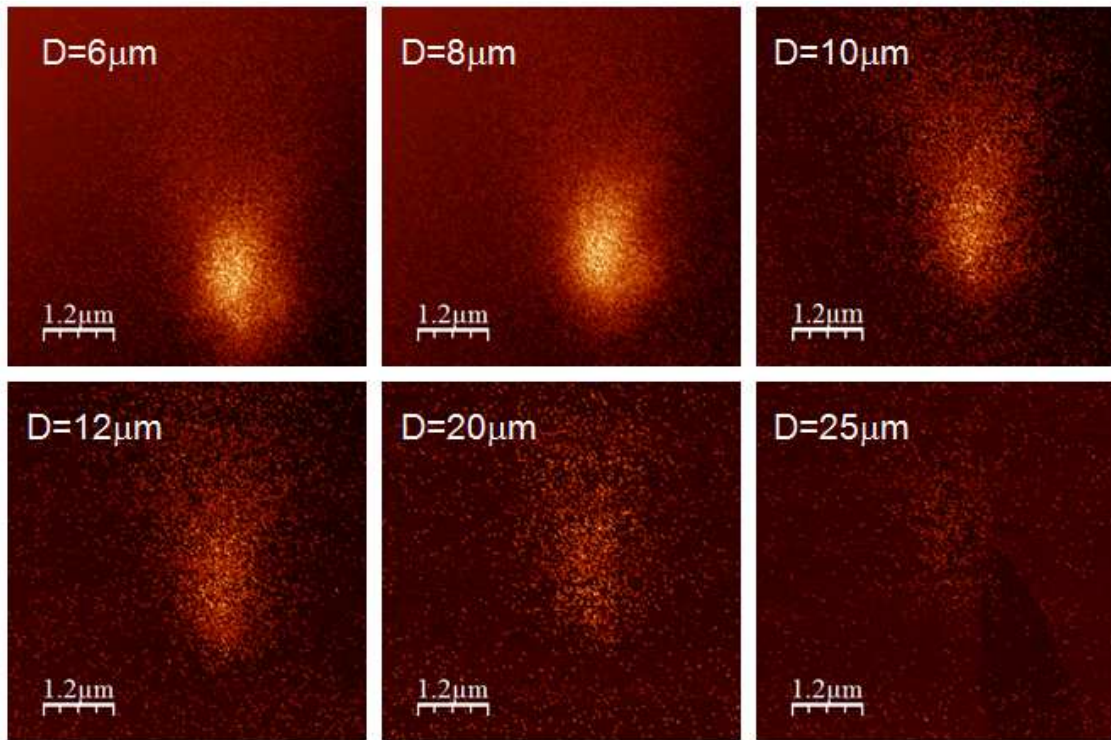


Figure 46. 6x6 μm NSOM scans of waveguided intensity as a function of distance, D , from the generation site. The limit, to first order, appears to be between 25-30 μm .

b. *Estimation of Absorption Coefficient*

Figure 47 shows the best fit exponential and the waveguided maximum intensity as a function of distance from the generation site. The exponential best fit had an R^2 (R-Square) value of 0.9. The R^2 value is a statistics term that represents how successful the fit is at explaining the variation

in the data. In this case, the fit explains about 90% of the variation in the data. The absorption coefficient based on the best fit was $.193 \mu\text{m}^{-1}$ or $\sim 2000 \text{ cm}^{-1}$. This order of magnitude seems reasonable for a ZnO nanowire of bandgap 3.26 eV, based on absorption coefficient measurements for thin film ZnO in Figure 48 [29]. Figure 49 shows this photon energy dependent absorption coefficient on a natural log scale.

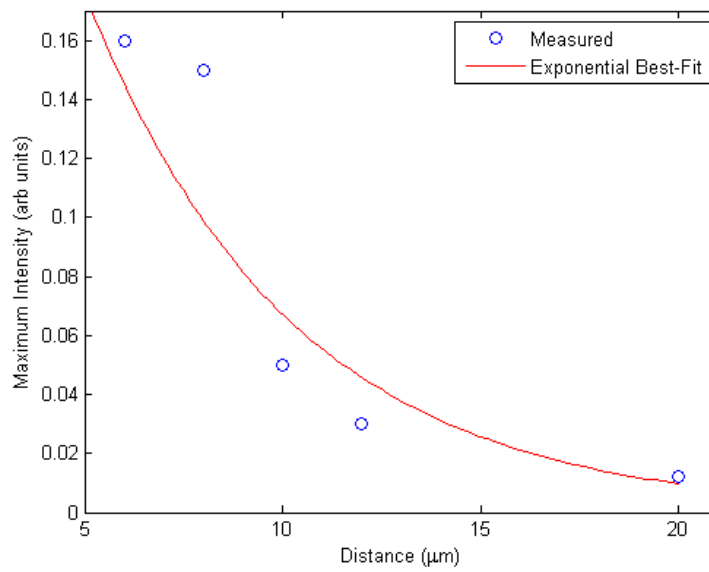


Figure 47. Maximum intensity waveguided as a function of distance between electron beam and end of nanowire.

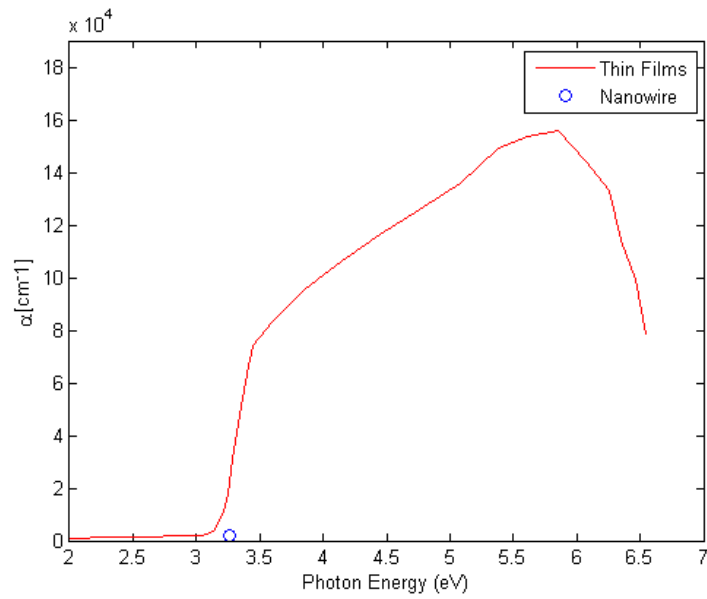


Figure 48. Plot of absorption coefficient (cm^{-1}) versus photon energy (eV) for ZnO thin films (red) and the ZnO nanowire estimation (blue). After [34].

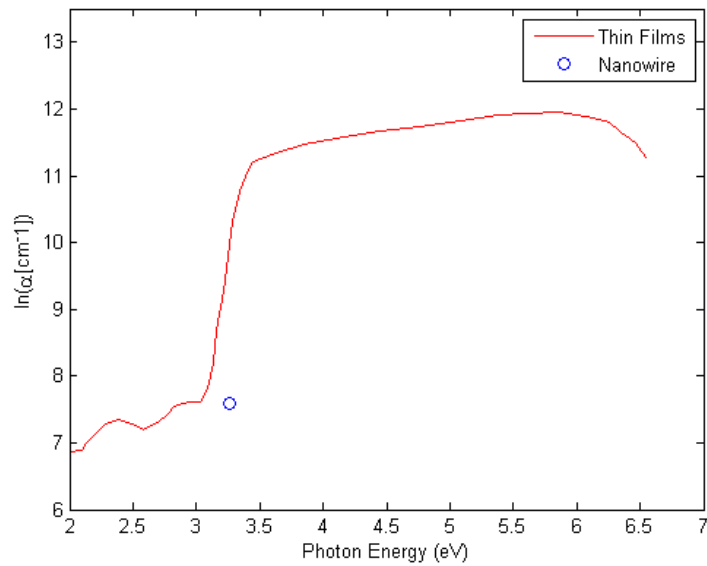


Figure 49. Plot of natural log of the absorption coefficient (cm^{-1}) versus photon energy (eV) for ZnO thin films (red) and the ZnO nanowire estimation (blue). After [34].

VI. CONCLUSIONS AND SUGGESTIONS FOR FUTURE RESEARCH

A. CONCLUSIONS

The purpose of this thesis was to advance the novel near field microscopy work pioneered at the Naval Postgraduate School. This was accomplished by placing the multiview 2000 inside of a higher resolution SEM for transport imaging of nanostructures. The higher resolution SEM used a more narrow beam diameter, which allows for more precise placement of the electron beam. The method was also improved by grounding the sample and probe tip to the stage. By introducing a common ground, the SEM charging effects were reduced and prevented the tip from accidentally crashing into the sample surface during approaches. A significant contribution to the method was to filter the signal generated by inherent luminescence of the NSOM/AFM probe created by either direct excitation or electron beam scattering effects. The filters were effective at removing approximately 90% of the probe signal that could interfere with diffusion length measurements, particularly for nanowires of low luminescence. The filters preserved approximately 70% of the NSOM signal from the nanowires.

Another objective of this thesis was to use the improved methods to measure the diffusion length of ZnO nanowires and determine the correlation between excess carrier diffusion length and nanowire diameter. For the wires chosen, with diameters of 250–1400 nm, the diffusion length appeared to increase with thickness up to approximately 800 nm. Above 800 nm, the diffusion length seemed to be constant at about 1 μ m. The author believes that when the diameter of the wire is smaller than the diffusion length, then the surface to volume ratio may contribute to increased surface effects, thereby limiting carrier transport. As the literature only had one such study on the diameter dependency on ZnO nanowire diffusion length, these results contribute

to the available data and can eventually aid in modeling the role of the surface in limiting carrier lifetime and diffusion lengths.

The thesis also sought to study the waveguiding phenomenon in ZnO nanowires. The author was able to observe the waveguiding output and measure the variation in the width of the distribution as a function of spot size (probe current), which corresponds to the local excitation rate in the nanostructure. As the probe current increased, as expected, the intensity of the light exiting the nanowires increased. However, the FWHM of the distribution was not correlated with spot size. The author observed no reduction in FWHM, which would be expected during a transition to lasing behavior. In studying the waveguiding phenomenon in ZnO nanowires, a first order estimate of the waveguiding limit and absorption coefficient was made. The waveguiding limit for 380 nm wavelength light propagation was approximately 20-30 μm , indicating an absorption coefficient of approximately 2000 cm^{-1} .

B. SUGGESTIONS FOR FUTURE RESEARCH

1. Reducing Charging and Drifting in SEM

There is room for further advancement in the NSOM/AFM method. The efforts to ground the sample and probe have not entirely eliminated the drifting and charging effects that tend to move the electron beam over the course of a scan. This is particularly important in maintaining the electron beam on more narrow nanowires. Any efforts to reduce charging and drifting of the SEM beam would improve the accuracy and limitations of the current configuration.

2. Linking the ZnO Nanowire Diffusion Length Diameter Dependency Work

Another area of advancement is measuring the diffusion length for wires of diameter between 60 nm and 250 nm. This would help make a more complete picture and perhaps link the previous work and this thesis on ZnO nanowire

diffusion length diameter dependency. More diameter dependent diffusion length measurements would help in understanding and modeling the role of the surface in limiting carrier transport.

3. Exploring Additional Materials.

The method could be applied to other direct bandgap semiconductors. Taking diffusion length measurements and studying waveguiding in other materials would provide a basis of comparison for this and other work. Of particular interest would be Gallium Nitride (GaN) nanowires, which are also being studied for UV lasers and sensors, and other III-V materials (such as gallium arsenide (GaAs) and indium phosphide (InP)).

THIS PAGE INTENTIONALLY LEFT BLANK

LIST OF REFERENCES

- [1] P. Gelsinger. (2006, September). *Moore's Law-The Genius Lives On* [Online]. Available: http://web.archive.org/web/20070713083830/http://www.ieee.org/portal/site/sscs/menuitem.f07ee9e3b2a01d06bb9305765bac26c8/index.jsp?&pName=sscs_level1_article&TheCat=2165&path=sscs/06Sept&file=Gelsinger.xml.
- [2] M. Kaku. (2010, April 24). *The Future of Computing (Fast, Cheap, and Invisible)* [Online]. Available: <http://bigthink.com/ideas/the-future-of-computing-power-fast-cheap-and-invisible?page=all>.
- [3] Wikipedia. *Moore's Law* [Online]. Available: http://en.wikipedia.org/wiki/Moore's_law
- [4] Z. Z. Bandic *et al.*, "Electron diffusion length and lifetime in p-type GaN," *Appl. Physics Lett.*, vol. 73, no. 22, pp. 3276–3278, Nov.1998.
- [5] J. Sarkar *et al.*, "Nanowires: Properties, applications and synthesis via porous anodic aluminum oxide template," *Bulletin Material Sci.*, vol. 30, no. 3, pp. 271–290, Jun., 2007.
- [6] Y. Li *et al.*, "One-dimensional metal oxide nanotubes, nanowires, nanoribbons, and nanorods: Synthesis, characterizations, properties and applications," *Critical Reviews in Material Sci.*, vol. 37, pp. 1–74, Mar. 2012.
- [7] J. Wang *et al.*, "Highly polarized photoluminescence and photodetection from single indium phosphide nanowires," *Science*, vol. 293, pp.1455–1457, 2001.
- [8] S. J. Tans *et al.*, "Individual single-wall carbon nanotubes as quantum wires," *Nature*, vol. 386, pp. 474–477, 1997.
- [9] S. J. Tans *et al.*, "Room temperature transistor based on a single carbon nanotube," *Nature*, vol. 393, pp. 49–52,1998.
- [10] D. N. Davydov *et al.*, "Field emitters based on porous aluminum oxide templates," *J. Appl. Physics*, vol. 86, pp. 3983–3987, 1999.
- [11] S.W. Chung *et al.*, "Silicon nanowire devices," *Appl. Physics Lett.*, vol. 76, pp. 2068–2070, 2000.
- [12] X. Duan *et al.*, "Indium phosphide nanowires as building blocks for nanoscale electronic and optoelectronic devices," *Nature*, vol. 409, pp. 66–69, 2001.

- [13] Y. Cui *et al.*, "Nanowire nanosensors for highly sensitive and selective detection of biological and chemical species," *Science*, vol. 293, pp. 1289–1292, 2001.
- [14] J. Knowles. (2002, March 12). *Warfare* [Online]. Available: <http://www.pcmag.com/article2/0,2817,509,00.asp>.
- [15] I. Test. (2012, April). *Tactical Gear Developments for Lessening Soldiers' Loads, Reducing Injuries* [Online]. Available: <http://ezinearticles.com/?Tactical-Gear-Developments-for-Lessening-Soldiers-Loads,-Reducing-Injuries&id=7027079>.
- [16] U.S. Army Soldier Systems Center. (2004, January). *The Warrior: Weighed Down* [Online]. Available: <http://www.natick.army.mil/about/pao/pubs/warrior/04/janfeb/index.htm>.
- [17] B. Hect *et al.*, "Scanning near-field optical microscopy with aperture probes: Fundamentals and applications," *The J. of Chemical Physics*, vol. 112, no. 18, pp. 7761–7774, May 2000.
- [18] H. Hallen. *North Carolina State University: The Optics Laboratory* [Online]. Available: <http://www.physics.ncsu.edu/optics/nsom/NSOMintro.html>.
- [19] R. A. Wilson and H. A. Bullen. *Basic Theory: Atomic Force Microscopy* [Online]. Available: http://asdlb.org/onlineArticles/ecourseware/Bullen/SPMModule_BasicTheoryAFM.pdf
- [20] Nanonics Imaging Ltd. *Multiview 2000* [Online]. Available: <http://www.nanonics.co.il/files/d670fe19442ca20f4ca99f58429602ea.pdf>
- [21] B. Yacobi and D. Holt, *Cathodoluminescence Microscopy of Inorganic Solids*, 1st ed. New York: Plenum Press, 1990, pp. 1–50.
- [22] B. Kasap, *Principles of Electronic Materials and Devices*, 3rd ed. New York: McGraw-Hill, 2007, pp. 373–427.
- [23] Warwick Department of Physics. *Electronic Band Structure* [Online]. Available: <http://www2.warwick.ac.uk/fac/sci/physics/current/postgraduate/regs/mpags/ex5/bandstructure>.
- [24] G. Sun, *Advances in Laser and Electro Optics: The Intersubband Approach to Si-based Lasers*, 1st ed. New York: InTech, 2010, pp. 1-20.
- [25] Z. Wang, "Novel nanostructures of functional oxides synthesized by thermal evaporation," *Advanced Functional Materials*, vol. 13, no. 1, pp. 9–24, Jan. 2003.

- [26] B. Kasap, *Principles of Electronic Materials and Devices*, 3rd ed., New York: McGraw-Hill, 2007, pp. 373–427.
- [27] *Multiview 2000 User Guide*, Jerusalem, Israel: Nanonics Imaging Ltd., 2010, pp. 09–75.
- [28] R.A. Cole, "Near field imaging of charge transport in gallium nitride and zinc oxide nanostructures," M.S. thesis, Physics Dept., Naval Postgraduate School, Monterey, CA, 2010.
- [29] O. Madelung, *Semiconductors Data Handbook*, 3rd ed. New York: Springer, 2004, ch. D, sec. 14, p. 434.
- [30] A. Soudi *et al.*, "Diameter dependence of the minority carrier diffusion length in individual ZnO nanowires," *Appl. Physics Lett.*, vol. 96, pp. 253115-1–253115-3, 2010.
- [31] L.G.Baird, "Near field imaging of gallium nitride nanowires for characterization of minority carrier diffusion," M.S. thesis, Physics Dept., Naval Postgraduate School, Monterey, CA, 2009.
- [32] P.J. Pauzauskie and P. Yang. *Nanowire photonics*. Available: http://www.cchem.berkeley.edu/pdygrp/pub_files/pubpdf/130.pdf.
- [33] M.H. Huang *et al.*, "Room-temperature ultraviolet nanowire nanolasers," *Sci.*, vol. 292, no. 5523, pp. 1897–1899, June 2001.
- [34] Z. R. Khan *et al.*, "Optical and structural properties of ZnO thin films fabricated by sol-gel method," *Materials Sci. and Applications*, vol. 2, pp. 340–345, Mar. 2011.

THIS PAGE INTENTIONALLY LEFT BLANK

INITIAL DISTRIBUTION LIST

1. Defense Technical Information Center
Ft. Belvoir, Virginia
2. Dudley Knox Library
Naval Postgraduate School
Monterey, California
3. Professor Andres Larraza
Chair, Department of Physics
Naval Postgraduate School
Monterey, California
4. Professor Nancy M. Haegel
Naval Postgraduate School
Monterey, California
5. Anree Little
Naval Postgraduate School
Monterey, California
6. Daniel Chisholm
Naval Postgraduate School
Monterey, California
7. David Lewis
Nanonics Imaging, Ltd.
Jerusalem, Israel